


RESEARCH ARTICLE

Open Access



Real-time imaging of mitochondrial redox reveals increased mitochondrial oxidative stress associated with amyloid β aggregates in vivo in a mouse model of Alzheimer's disease

Maria Calvo-Rodriguez^{1,3} , Elizabeth K. Kharitonova¹, Austin C. Snyder¹, Steven S. Hou¹, Maria Virtudes Sanchez-Mico¹, Sudeshna Das¹, Zhanyun Fan¹, Hamid Shirani², K. Peter R. Nilsson², Alberto Serrano-Pozo¹ and Brian J. Bacskai^{1*}

Abstract

Background Reactive oxidative stress is a critical player in the amyloid beta ($A\beta$) toxicity that contributes to neurodegeneration in Alzheimer's disease (AD). Damaged mitochondria are one of the main sources of reactive oxygen species and accumulate in $A\beta$ plaque-associated dystrophic neurites in the AD brain. Although $A\beta$ causes neuronal mitochondria reactive oxidative stress in vitro, this has never been directly observed in vivo in the living mouse brain. Here, we tested for the first time whether $A\beta$ plaques and soluble $A\beta$ oligomers induce mitochondrial oxidative stress in surrounding neurons in vivo, and whether this neurotoxic effect can be abrogated using mitochondria-targeted antioxidants.

Methods We expressed a genetically encoded fluorescent ratiometric mitochondria-targeted reporter of oxidative stress in mouse models of the disease and performed intravital multiphoton microscopy of neuronal mitochondria and $A\beta$ plaques.

Results For the first time, we demonstrated by direct observation in the living mouse brain exacerbated mitochondrial oxidative stress in neurons after both $A\beta$ plaque deposition and direct application of soluble oligomeric $A\beta$ onto the brain, and determined the most likely pathological sequence of events leading to oxidative stress in vivo. Oxidative stress could be inhibited by both blocking calcium influx into mitochondria and treating with the mitochondria-targeted antioxidant SS31. Remarkably, the latter ameliorated plaque-associated dystrophic neurites without impacting $A\beta$ plaque burden.

Conclusions Considering these results, combination of mitochondria-targeted compounds with other anti-amyloid beta or anti-tau therapies hold promise as neuroprotective drugs for the prevention and/or treatment of AD.

Keywords Oxidative stress, ROS, Alzheimer's disease, Mitochondria, SS31, Neurodegeneration, Multiphoton microscopy

*Correspondence:

Brian J. Bacskai

BBACSKAI@mgh.harvard.edu

Full list of author information is available at the end of the article



© The Author(s) 2024. **Open Access** This article is licensed under a Creative Commons Attribution 4.0 International License, which permits use, sharing, adaptation, distribution and reproduction in any medium or format, as long as you give appropriate credit to the original author(s) and the source, provide a link to the Creative Commons licence, and indicate if changes were made. The images or other third party material in this article are included in the article's Creative Commons licence, unless indicated otherwise in a credit line to the material. If material is not included in the article's Creative Commons licence and your intended use is not permitted by statutory regulation or exceeds the permitted use, you will need to obtain permission directly from the copyright holder. To view a copy of this licence, visit <http://creativecommons.org/licenses/by/4.0/>. The Creative Commons Public Domain Dedication waiver (<http://creativecommons.org/publicdomain/zero/1.0/>) applies to the data made available in this article, unless otherwise stated in a credit line to the data.

Background

Alzheimer's disease (AD) is a progressive, neurodegenerative disorder that leads to dementia. The main neuropathological hallmarks of AD are the deposition of extracellular amyloid beta (A β) plaques and intraneuronal neurofibrillary tangles, as well as multiple cellular changes, including neuronal and synapse loss, synaptic dysfunction, mitochondrial structural and functional abnormalities, and inflammatory responses. While the FDA has recently approved an anti-A β antibody as the first therapy targeting the fundamental pathophysiology of the disease [1, 2], unfortunately, there is still an urgent necessity of drugs that can prevent or slow down AD clinical progression.

Mitochondrial dysfunction is considered an early event in the AD pathophysiologic process. Besides providing ATP, mitochondria play several key roles, including synaptic maintenance, intracellular calcium (Ca²⁺) signaling regulation, free radical production and scavenging, and activation of caspases. An immediate consequence of mitochondrial dysfunction is the increase of reactive oxygen species (ROS) production, a byproduct of the electron transport chain, that promotes oxidative damage to DNA, RNA, proteins, and lipids. Mitochondria are both one of the main cellular sources of ROS, and one of the targets of ROS toxicity. Oxidative stress results from an imbalance between pro-oxidants and antioxidants; neurons hamper mitochondrial oxidative stress with cellular antioxidant defenses and, in severe cases, removing damaged mitochondria via mitophagy [3]. These systems regulate the cellular reduction/oxidation (redox) balance, and thereby, neuronal survival. However, when mitochondria are severely damaged, a vicious cycle can be triggered whereby the antioxidant defense decreases, thus increasing the production of ROS (which further damages mitochondria), enhancing free radicals' generation, and reducing or depleting the antioxidant capacity.

Oxidative damage and mitochondrial degeneration are implicated in AD pathophysiology. For instance, the level of antioxidant enzymes is decreased in plasma from AD patients, leading to an accumulation of oxidative damage [4]. AD pathogenesis is correlated with increased oxidative stress levels due to enhanced production of ROS and/or decreased antioxidant defense mechanisms [5]. However, whether oxidative stress is the cause or consequence of AD neuropathological changes and whether changes in the redox homeostasis have a direct impact on the progression of AD pathology remain open questions. Recently, mitochondria-targeted molecules have been developed and tested as neuroprotective drugs for AD [6, 7]. However, to date no studies have directly visualized the effects of A β aggregates on mitochondrial redox state in vivo, and

whether this can be abrogated using mitochondria-targeted antioxidants.

To address these questions, we used a combination of a genetically encoded fluorescent redox sensor and multiphoton microscopy to image and monitor in vivo the mitochondrial redox imbalance in neurons from the APP/PS1 transgenic (Tg) mouse model of AD. We demonstrate that A β plaque deposition, and particularly soluble oligomeric A β species, lead to increased mitochondrial oxidative stress levels within neuronal mitochondria. We also show that inhibiting mitochondrial Ca²⁺ influx, which is pathologically exacerbated in these A β plaque-depositing mice [8] can prevent this mitochondrial redox dysregulation in neurons. Lastly, we demonstrate that the use of antioxidants directly targeting mitochondria is effective at decreasing mitochondrial oxidative stress to basal levels and reverting A β plaque-associated dystrophic neurites in these AD mice, supporting the idea that mitochondria-targeted compounds that prevent or minimize mitochondrial dysfunction could hold promise as neuroprotective drugs against AD progression, and could be used in combination with other anti-amyloid beta and/or anti-tau therapies.

Materials and methods

Animals

Animal experiments were performed under the guidelines of the Institutional Animal Care and Use Committee (IACUC, protocol #2018N000131). All experimental procedures were approved by the Institutional Animal Care and Use Committee at Massachusetts General Hospital. The following transgenic lines were used: APP^{swe}/PSEN1 Δ E9 double Tg mice (heretofore APP/PS1) (The Jackson laboratory, B6.Cg-Tg(APP^{swe},PSEN1 Δ E9)85Dbo/Mmjax, MMRRC Cat# 034832-JAX, RRID:MMRRC_034832-JAX) (APP/PS1, 2- to 3-months of age (young) and 8- to 10-months of age (adult) of either sex, expressing both human *APP* gene carrying the Swedish mutation and exon 9 deletion mutation in the *PS1* gene, and age-matched non-transgenic littermates (Wt) were used as controls; and C57BL/6 J males (4- to 5-months of age, Charles River) for the application of DTT and DTDP, conditioned media and Ru360. For conditioned media preparation, Tg2576 males (Taconic Farms, B6;SjL-Tg(APP^{swe})2576Kha, IMSR Cat# TAC:1349, RRID:IMSR_TAC:1349), which heterozygously overexpress human APP^{swe} under the PrP promoter, were mated with Wt females for preparation of primary cortical neurons. Mice were socially housed with up to four animals per cage, with ad libitum access to food and water, in a 12-h light/dark cycle and controlled temperature and humidity conditions. A sample size of

at least 3 mice (of either sex) was randomly allocated to experimental groups.

Cell culture

Mouse neuroblastoma cells (N2a) were grown at 37°C in a humidified incubator chamber under 5% CO₂ in Opti-MEM (Gibco), supplemented with 5% fetal bovine serum (FBS) (Atlanta Biologicals), 1% penicillin, and 1% streptomycin (Gibco). Cells were plated into 8-well chamber slides (Sarstedt) at a density of 30,000 cells/well and transiently transfected using Lipofectamine 2000 (Life Technologies) according to the manufacturer's instructions and imaged 24 h later.

Primary cortical neurons were prepared as previously described [8]. Briefly, neurons were obtained from embryonic day 14 (E14) CD1 (Charles Rives Laboratories) mouse embryos. Neurons were dissociated using Papain dissociation system (Worthington Biochemical Corporation, Lakewood, NJ, USA). Cells were plated in 8-well chamber slides previously coated with poly-D-lysine at a density of 30,000 cells/well and were maintained for 10–14 days in vitro (DIV) in Neurobasal medium supplemented with 2% B27 (Gibco), 1% penicillin/streptomycin (Gibco) and 1% glutamax (Gibco) in a humidified 37°C incubator with 5% CO₂ without further media exchange. Neurons were either transfected using Lipofectamine 2000 (Life Technologies) or infected with AAV.hSyn.mt-roGFP after 12–14 DIV, and imaged 1 or 3 days later respectively. Experiments were performed after a culturing period of 12–14 DIV.

Plasmids

mRuby-Mito-7 was a gift from Michael Davidson (Addgene plasmid #55,874; <http://n2t.net/addgene:55874>; RRID:Addgene_55874). mRuby-ER-5 was a gift from Michael Davidson (Addgene plasmid #55,860; <http://n2t.net/addgene:55860>; RRID:Addgene_55860). Matrix-roGFP (mt-roGFP) was a gift from Paul Schumacker (Addgene plasmid #49,437; <http://n2t.net/addgene:49437>; RRID:Addgene_49437).

AAV.hsyn.mt-roGFP construction and production

DNA sequence of mt-roGFP [9] was ligated between the inverted terminal repeat sites (ITRs) of an adenovirus (AAV, serotype 2/8) packaging plasmid with human synapsin (hSyn) promoter, and the WPRE/SV40 sequence. Thus, the expression cassette included the following components: (1) a 1.7-kb sequence containing human synapsin 1 gene promoter, (2) mt-roGFP, (3) WPRE, and (4) Simian virus 40 (SV40). Human embryonic kidney (HEK) 293 T cells were co-transfected with the construct and a helper plasmid and harvested. Virus was purified

and titrated by infecting HEK293T cells. Virus titer was 1.0×10^{12} viral genome copies per mL.

SS31 preparation and drug delivery

SS31 (D-Arg-Dmt-Lys-Phe-NH₂; Dmt = 2,6'-dimethyltyrosine) and SS20 (Phe-D-Arg-Phe-Lys-NH₂) were obtained from Biomatik (<https://www.biomatik.com>). SS31 and SS20 were administered intraperitoneally to APP/PS1 Tg and non-transgenic littermate mice (5 mg/kg body weight) twice a week for 8 weeks. The treatment began when the mice were 8 months of age, and the imaging sessions were carried out at 10 months of age. All mice were daily observed by a veterinarian. SS31 dose was determined based on previous studies [10, 11], suggesting that this concentration had the maximum protective effects without any adverse side-effects or toxicity.

Preparation of Wt and Tg neuronal conditioned media and Aβ-immunodepleted media, and measurement of soluble Aβ levels

Primary cortical neuron cultures from Tg2576 mice, heterozygous for the hAPP^{sw} mutation, were prepared as explained above. Tissue from each individual embryo was collected for genotyping. Primary neurons were maintained in Neurobasal media containing 2% B27 supplement, 1% penicillin/streptomycin and 1% Glutamax. Conditioned media from either Tg cultures (TgCM) or Wt littermates (WtCM) was collected at 14 DIV. Measurement of soluble Aβ levels were conducted using sandwich ELISA as previously described [8]. Briefly, CM was collected from the primary cultures, and Aβ₁₋₄₀ was measured with commercial colorimetric ELISA kit (WAKO, Wako #294–64,701 Human/Rat Aβ₁₋₄₀), specific for human. A 96-well plate reader was used, following the manufacturer's instructions. Each sample was run in duplicates. Protein concentrations of the CM were determined and Aβ was expressed in nM. Additionally, human Aβ was immunodepleted from TgCM with the mouse monoclonal antibody 6E10 (Purified anti-β-Amyloid, 1–16 antibody BioLegend Cat# 803,004, RRID: AB_2715854) and Protein G Sepharose beads (Sigma-Aldrich). Protein G beads were conditioned with cold Neurobasal media. 1 mL of TgCM and 40 μL of the pre-conditioned G beads were incubated with 6 μg of 6E10 antibody overnight at 4°C under rotation. Supernatant was collected and Aβ concentration quantified by colorimetric ELISA human/rat Aβ₁₋₄₀. Aβ₁₋₄₀ concentration in the media were 0.3 nM for WtCM, 5 nM for TgCM and 0.7 nM for Aβ-immunodepleted TgCM, demonstrating an efficient immunodepletion of Aβ from the TgCM. The concentration of Aβ₀ in the TgCM has been shown to represent around 10% of the total amount of Aβ₁₋₄₀ [12].

Stereotactic intracortical injection of AAV.hSyn.mt-roGFP

For acute experiments, AAV.hSyn.mt-roGFP was injected into 4–5-month old C57BL/6 J6 Wt mice somatosensory cortex, as previously described [13]. Mice were anesthetized using 5% isoflurane (vol/vol) for induction and maintained at 1.5% throughout the surgery. Under a stereotactic frame (Kopf Instruments), a burr hole was drilled in the skull at 1 mm anteroposterior, 1 mm mediolateral from bregma, and AAV was injected at -0.8 mm dorsoventral. A programmable syringe pump with a 33-gauge sharp needle attached to a 10 μ L Hamilton micro-syringe was used for infusion. 3 μ L of viral suspension were injected at 0.15 μ L/min. Body temperature was maintained throughout surgery with a heating pad. After injection, the needle was removed, and the mouse scalp sutured. Mice were put on a heating pad for recovery. For stable fluorescent expression, mice were imaged 3 weeks after injection.

For chronic experiments, AAV.hSyn.mt-roGFP was injected to 9 mo-old or 3 mo-old Tg mice in the somatosensory cortex at the moment of the cranial window implantation. Mice were given buprenorphine (0.1 mg/kg) for 3 days following surgery.

Cranial window implantation

Mice were anesthetized with isoflurane, the scalp shaved and sterilized, and an incision was made to expose the underlying skull. A custom-made stereotax fixed the skull. For chronic windows, an area of skull no larger than 5-mm was removed and replaced with a glass coverslip for imaging. After craniotomy, mice were placed on a heating pad for recovery and two-photon imaging was performed 3 weeks later. For acute windows (in vivo validation and CM experiments), dura matter was removed, and 8-mm windows were implanted. Two-photon imaging was performed immediately after cranial window implantation. Mice were given buprenorphine (0.1 mg/kg) for 3 days following surgery.

In vivo multiphoton microscopy imaging

HS169 (10 mg/kg) was retro-orbitally injected 24 h before the imaging session to label A β plaques [14]. Texas Red Dextran (70,000 MW; 12.5 mg/mL in PBS; Molecular Probes) was retro-orbitally injected immediately prior to the imaging session to provide a fluorescent angiogram. Mice were anesthetized by isoflurane and head-restrained using a custom made stereotax. Images of AAV.hSyn.mt-roGFP were acquired on an Olympus FluoView FV 1000MPE multiphoton laser-scanning system mounted on an Olympus BX61WI microscope and equipped with a 25 \times Olympus water immersion objective (1.05 numerical aperture (NA)). A Deep-See Mai Tai Ti:Sapphire mode-locked laser (Spectra-Physics)

was used for multiphoton excitation at the following wavelengths: 800 and 900 nm for AAV.hSyn.mt-roGFP, 800 nm for HS169 and 900 nm for Texas Red Dextran. Emitted fluorescence was collected in three channels in the range of 460–500, 520–560 and 575–630 nm. All images were obtained at depths up to 200 μ m from the pial surface, and were captured at a 5 \times digital zoom. Five to eight cortical volumes (Z-series, 127 μ m \times 127 μ m) were acquired per mouse, at a step size of 2 μ m and a resolution of 512 \times 512 pixels. Photomultiplier settings remained unchanged throughout the different imaging sessions. Laser power was adjusted as needed to avoid image saturation and kept always below 30 mW to avoid phototoxicity.

For acute CM experiments and in vivo validation of AAV.hSyn.mt-roGFP, an imaging session was first performed to determine the basal resting ratio 800/900. Then, the window was opened and sealed again after application of DTT, DTDP, WtCM, TgCM, A β -immunodepleted TgCM, Ru360 (Calbiochem, Merck Millipore) or Ru360 + TgCM (40 μ L final volume applied). Ru360 was preincubated for 15 min before application of TgCM. After either 20 min (for validation) or 1 h (for CM experiments), the same fields of view were reimaged to determine the relative changes in ratio 800/900 ($\Delta R/R_0$). The fluorescent angiogram created by Texas Red Dextran helped with re-locating the same fields of view.

Image processing and quantification

RoGFP displays two excitation peaks that are sensitive to redox changes. The redox status is assessed by monitoring the ratio of GFP fluorescence emission at 800 and 900 nm excitation [15, 16]. For the analysis of mitochondrial redox state in primary neurons, ROIs were drawn around somas and primary processes as well as in background regions outside cells. Pixel intensity was measured on images taken at two wavelengths (800 and 900 nm), and background subtracted. To calculate the fluorescent intensity ratios, the 800 nm image was divided by the 900 nm image in a pixel-by-pixel manner.

All multi-photon images were analyzed using customized MATLAB scripts (MathWorks). To perform automatic segmentation of mitochondria, an adaptive thresholding procedure was applied to the in vivo images (acquired at 5 \times digital zoom) to generate binary images and individual mitochondria were identified in neuronal somas and processes using a constraint on object size. A β plaques were manually extracted from the z-stacks. Background was subtracted from the 800 and 900 nm channel images. The ratio value of each segmented mitochondria was determined by taking of the sum of the pixels within the segmented region in the 800 nm channel and dividing it by the sum in the 900 nm channel. Pseudocolored

images were generated using MATLAB by first creating the ratio image by dividing the 800 nm image by the 900 nm image on a pixel-by-pixel basis. Next, the ratio image was assigned to the RGB (Red, Green, Blue) color space with the color range determined by the maximal achievable redox changes that can be accomplished with DTT and DTDP treatment in vivo. The RGB image was then converted to the HSV (Hue, Saturation, Value) color space with the Value field being set to the overall intensity image (800 nm + 900 nm channels). Distance to A β plaque was measured based on the centroid of the mitochondrion to the edge of the nearest plaque. Images presented in the figures are a single slice from the z-stacks.

Immunohistochemistry

Mice were euthanized by CO₂ asphyxiation and transcardially perfused with 20 mL of PBS followed by 20 mL of 4% PFA. Brains were extracted and kept in a fixing solution (4% PFA and 30% glycerol in PBS) for 24 h, and then embedded in OCT. The OCT block was then sectioned into 20 μ m coronal sections on a cryostat (Leica). Sections were first subjected to antigen retrieval, by heating with citrate buffer with Tween20 at pH 6.0, and then permeabilized with 0.5% Triton X-100, blocked with 5% normal goat serum, and incubated with target antibodies at 4°C o/n (GFP (1:500, Antibodies Incorporated Cat# GFP-1020, RRID:AB_10000240), HSP60 (1:200, Abcam Cat# ab46798, RRID:AB_881444), GS (1:500, Abcam Cat# ab73593, RRID:AB_2247588), NEUN (1:500, R&D Systems Cat# MAB377, RRID:AB_2298767), A β (1:500, Immuno-Biological Laboratories Cat# 18,584, RRID:AB_10705431), Neurofilament SMI312F (1:1000, BioLegend Cat# 837,904, RRID:AB_2566782). Corresponding secondary antibodies (Alexa Fluor 488 1:1000 (Molecular Probes Cat# A-11039, RRID:AB_142924), Alexa Fluor 647 1:1000 (Molecular Probes Cat# A-21245, RRID:AB_141775 and Molecular Probes Cat# A-21235, RRID:AB_2535804), Alexa Fluor 594 1:1000 (Molecular Probes Cat# A-11012, RRID:AB_141359), Cy3 1:1000 (Molecular Probes Cat# A-11039, RRID:AB_142924 and Abcam Cat# ab6939, RRID:AB_955021), Cy5 1:1000 (Abcam Cat# ab97035, RRID:AB_10680176 and Jackson ImmunoResearch Labs Cat# 111-175-144, RRID:AB_2338013) were applied and incubated for 1 h at room temperature. Appropriate sections were treated with 1% ThioS, and/or cover slipped with anti-fade mounting medium with DAPI (Vector Laboratories, (H1500)).

Confocal microscopy

Imaging of immunostained sections ((GFP, HSP60, NeuN, GS), and (A β , NF)) was conducted on an Olympus Fluoview 3000 confocal microscope with a

40 \times immersion objective. Applicable laser excitation wavelengths were used for optimal fluorophore excitation and emission separation and detection. Parameters were maintained for all slides within each antibody condition.

Fluorescence imaging

For A β plaque burden analysis (A β immunohistochemistry and ThioS staining), slides were scanned using an Olympus VS120-S6-W virtual slide microscope. Images were taken with a 20 \times objective and analyzed using CellSens software (Olympus). A manual threshold was set to include both diffuse and dense-core plaques. These parameters were maintained constant throughout all image analyses and analyzed for total burden.

Analysis of publicly available human brain single RNA-seq datasets

The expression of 31 mitochondrial genes involved in mitochondrial antioxidant defense was compared in advanced AD Braak stages (V-VI) versus control subjects (Braak 0-I-II). Data were obtained from a public single-nucleus RNA-Seq (snRNA-seq) performed on dorsolateral prefrontal cortex samples from 48 individuals with varying levels of AD pathology [17]. The samples were grouped by Braak stage, which assesses the distribution of tau neurofibrillary tangles in the subject's brain [18]. Multiple comparisons corrections were performed using the Benjamini–Hochberg method [19]. For the purpose of selection for visual display, a false discovery rate (FDR) threshold of 0.25 was used.

Statistics

Graph Pad Prism (version 6.0) was used for statistical analyses and data presentation. Data are reported as mean \pm SEM. Either Mann–Whitney test or paired t-test were used to compare two different conditions. Kruskal–Wallis ANOVA followed by Dunn's multiple comparisons test were used to compare three or more different conditions (e.g., CM). Statistical correlations were determined using Pearson's correlation test. In each experiment, the number of animals, volumes, and statistical parameters can be found in the figure legend, together with the mean and standard error estimates and the p-values. $p < 0.05$ was considered statistically significant.

Results

hsyn.mt-roGFP targets mitochondria and reports oxidative stress changes in vitro and in vivo.

To study specific redox changes, we used the genetically encoded redox-sensitive fluorescent protein roGFP [13], which was targeted to the mitochondrial matrix (matrix-roGFP [9, 20, 21], heretofore mt-roGFP) by using the mitochondria-targeting sequence from

cytochrome oxidase subunit IV [9]. With this probe, the ratio of the fluorescence after excitation at 800 nm over the excitation at 900 nm (Ratio 800/900) reflects the redox environment, with an increase in ratio indicating oxidation. We chose this reporter because of its ratiometric properties (i.e., ratiometric by sequential excitation near its absorption maxima at 800 and 900 nm), which enables true quantitative redox imaging [22, 23]. RoGFP redox sensors almost exclusively report reduced/oxidized glutathione (GSH/GSSG) ratio [24], which is mediated by cell endogenous glutaredoxins. Additionally, roGFP has been described to be minimally affected by cellular pH and Cl^- changes in the physiological range [25, 26], unlike other ratiometric redox sensors such as Hyper [27], which senses H_2O_2 but markedly responds to pH changes [28]. Mt-roGFP is restricted to the mitochondrial matrix and is not associated with either cristae or peripheral mitochondrial membranes ([9] and Supplementary Fig. 1).

We first validated the sensor specificity in cultured N2a cells and primary mouse neurons by co-labeling with a different plasmid targeted to mitochondria. Colocalization of mt-roGFP and mRuby-mito7 confirmed the mitochondrial localization of mt-roGFP (Supplementary Fig. 1a). In addition, lack of colocalization between mt-roGFP and an endoplasmic reticulum (ER) marker (mRuby-ER5), co-transfected in N2a cells, further demonstrated the mitochondria-specific targeting of mt-roGFP (Supplementary Fig. 1b).

We then validated the sensor functionality in cultured primary mouse neurons by determining its responsiveness to reduction/oxidation. Primary neurons were exposed to saturating doses of the reductant DTT (dithiothreitol) or the oxidant DTDP (dithiodipyridine), to fully reduce or oxidize the cells respectively. As illustrated in Supplementary Fig. 1c and d, treatment with DTT resulted in an expected lower Ratio800/900 (indicating reducing conditions) due to an increase in fluorescence intensity at 900 nm (in green) and a decrease at 800 nm (in red); whereas the oxidizing conditions of DTDP treatment led to opposite results (i.e., increased Ratio 800/900), indicating oxidative environment. The Ratio 800/900 distribution was slightly shifted to the left under DTT reducing conditions, indicating lower redox levels in the mitochondrial matrix (Supplementary Fig. 1d blue histogram), and greatly shifted to the right under DTDP oxidizing conditions (Supplementary Fig. 1d red histogram), indicating higher relative oxidized levels.

We next targeted this reporter to neurons by using the human synapsin promoter (hSyn) and packaging it into an adenoviral-associated vector (AAV.hSyn.mt-roGFP) (Fig. 1a). We validated its neuronal expression and mitochondrial localization by injecting it into the

somatosensory cortex of wild-type (Wt) living mice and co-staining with markers of neurons (NEUN, also known as RBFOX3), astrocytes (GS, glutamine synthetase) and mitochondria (HSP60, heat shock protein 60) upon mice euthanasia 3 weeks later. Supplementary Fig. 2 shows the exclusive localization of the vector to neuronal mitochondria (but not astrocytes), based on its colocalization with NEUN and HSP60. We chose the somatosensory cortex for our studies since somatosensory deficits have been reported in AD patients, as this area is affected early in the AD progression [29, 30]. Additionally, this area of the mouse brain is broadly used in research focusing on AD and involving in vivo multiphoton microscopy and mice [31]. Using an AAV targeted to the cytosol of neurons (roGFP), previous studies in our group have demonstrated increased cytosolic oxidative stress in the neurons of this brain area [16], as well as a general mitochondrial alterations surrounding plaques by using different dyes topically applied to the somatosensory cortex of the mouse [32]. We then tested whether it was possible to monitor dynamic changes in mitochondrial oxidative stress in neurons in vivo with the newly created AAV.hSyn.mt-roGFP reporter. Brains of wild-type (Wt) living mice were topically exposed to the reductant DTT or the oxidant DTDP through a craniotomy, to fully reduce or oxidize their neuronal mitochondria respectively, and their effects were imaged with multiphoton microscopy. Treatment with DTDP increased the relative oxidative stress levels within the mitochondria of neurons (represented as Ratio 800/900), whereas DTT did not alter the relative redox levels as measured by the sensor (Fig. 1b-d, and Supplementary Fig. 3). The corresponding histograms show a shift toward higher ratios upon hSyn.mt-roGFP oxidation with DTDP, but no change upon reduction with DTT (Fig. 1e, f), consistently with the greater effect of DTDP over DTT observed in vitro (Supplementary Fig. 1d). These data suggest that neuronal mitochondria are, in general, at their lower redox state in baseline conditions, so that application of a reducing agent has a minimal effect on their redox state. Alternatively, the dynamic range of this probe may be capped at low redox levels, which are not the scope of this study. Further studies in vivo would be necessary to understand this question.

However, these data demonstrate that hSyn.mt-roGFP sensor enables monitoring mitochondrial relative oxidized levels in cortical neurons in living mice. Therefore, we next extended these findings to a mouse model of cerebral β -amyloidosis.

Mitochondrial oxidative stress in neurons from AD transgenic mice after $\text{A}\beta$ plaque deposition.

We used the APP^{swe}/PSEN1 Δ E9 (APP/PS1) Tg mouse as a model of AD. This mouse model deposits

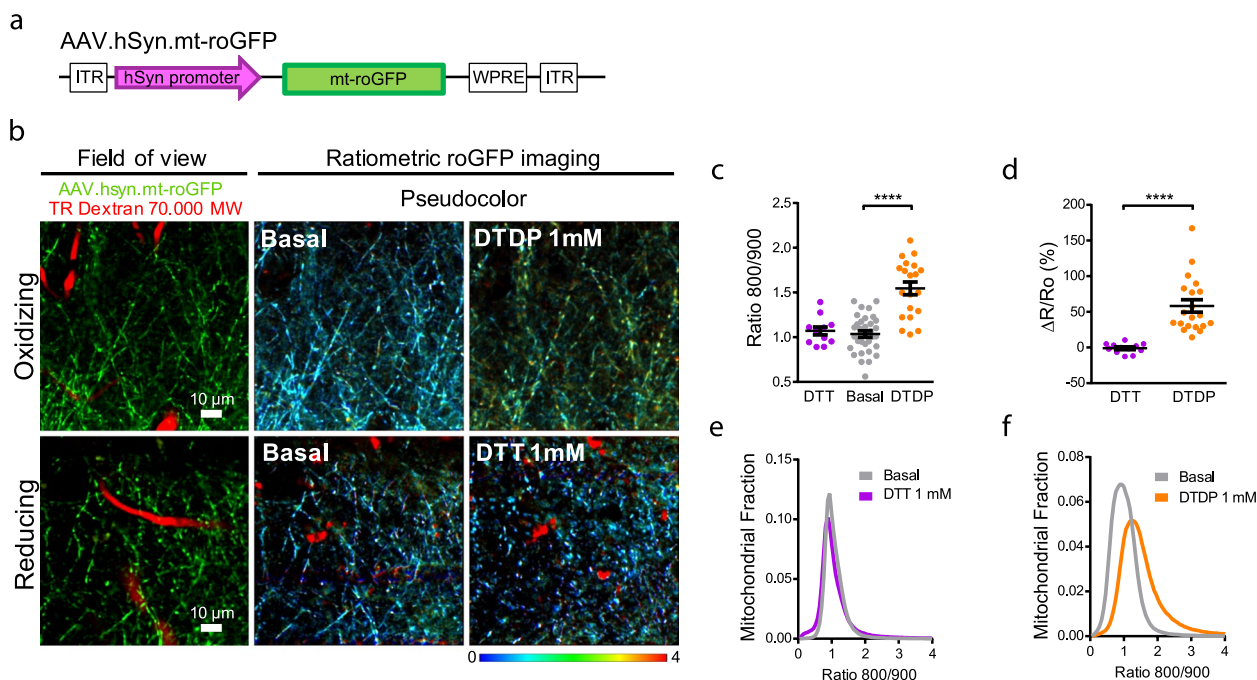


Fig. 1 AAV.hSyn.mt-roGFP expresses in neuronal mitochondria and is functional in vivo. **a** Diagram of construct of AAV.hSyn.mt-roGFP.WPRE. **b** Validation of pAAV.hSyn.mt-roGFP in vivo. 4-mo-old C57Bl/6 mice were intracortically injected with pAAV.hSyn.mt-roGFP and exposed to either the oxidant DTDP or the reducing agent DTT. Field of view shows two-photon images of the expression of the AAV (green) in the cortex of the C57Bl/6 J mice. Blood vessels are labelled with Texas Red (TR) Dextran 70,000 MW (red). Ratiometric roGFP imaging shows pseudocolor images according to the pseudocolor scale on the bottom, in basal conditions and after topical application of DTDP or DTT onto the brain surface. Scale bars represent 10 μ m. **c** Scatter dot plot represents the Ratio 800/900 in neuronal mitochondria of every volume acquired. Error bars represent mean \pm SEM. (Basal: 1.06 ± 0.036 , DTT: 1.07 ± 0.044 , DTDP: 1.55 ± 0.072 , **** $p < 0.0001$, $n = 33$, 12 and 20 z-stacks from 7, 3 and 4 mice respectively, all male). **d** Scatter dot plot represents the relative change (%) in ratio for each condition. Error bars represent mean \pm SEM (DTT: $-0.96 \pm 1.997\%$, $n = 12$ z-stacks; DTDP: $58.18 \pm 8.719\%$, $n = 20$ z-stacks from 3 and 4 male mice respectively, **** $p < 0.0001$). **e, f** Histograms of Ratio 800/900 frequency distribution in basal conditions (grey) and 20 min after application of DTT 1 mM (**e**, purple) and DTDP 1 mM (**f**, orange) in neurons

A β plaques starting at 5 months of age [33]. In order to analyze redox state changes due to A β aggregates, we first evaluated mitochondrial redox levels after A β plaque deposition. APP/PS1 Tg and non-Tg littermate mice were injected with AAV.hSyn.mt-roGFP followed by cranial window implantation (Fig. 2a). HS169 dye was injected IV 24 h before the imaging session to label A β plaques [14], and Texas Red Dextran was injected IV on the same day to create a fluorescent angiogram (Fig. 2b and Supplementary Fig. 4). We observed significant changes in the mitochondrial redox balance in neurons in the APP/PS1 Tg mouse compared to non-Tg mice (Fig. 2c, d, e), an effect that was more noticeable in male mice (Supplementary Fig. 5). To determine whether A β plaques impact mitochondrial oxidative stress levels in the surrounding neurons, a Pearson correlation between the Ratio 800/900 and the distance to the nearest A β plaque was performed (Fig. 2f). A negative correlation was observed between the two parameters (i.e., higher Ratio 800/900 closer to A β plaques), suggesting that A β plaques could trigger this increase

in mitochondrial oxidative stress. Interestingly, it could be noted that some of the mitochondria with the higher Ratio 800/900 (yellow to red colors in pseudocolor image 2b) surrounding A β plaques exhibit alterations in morphology, i.e., round shape and bigger size (swollen) or fragmented (Fig. 2b, APP/PS1), thus confirming their detrimental conditions. These findings are in line with previous reports from our own group and others, showing mitochondrial defects related to amyloid β plaques and soluble A β oligomers [8, 32, 34].

Since neurons are highly compartmentalized cells and might have different energy requirements in different compartments [35], we calculated and compared mitochondrial relative redox state in both somas and neurites independently (Fig. 2g-k). The mitochondrial redox state in neurites was significantly higher than in somas both for APP/PS1 Tg and non-Tg mice, with APP/PS1 Tg mice exhibiting higher oxidative stress in both compartments relative to non-Tg mice (Fig. 2h-k).

To unequivocally determine the role of A β as trigger of the observed increased oxidative stress in neuronal

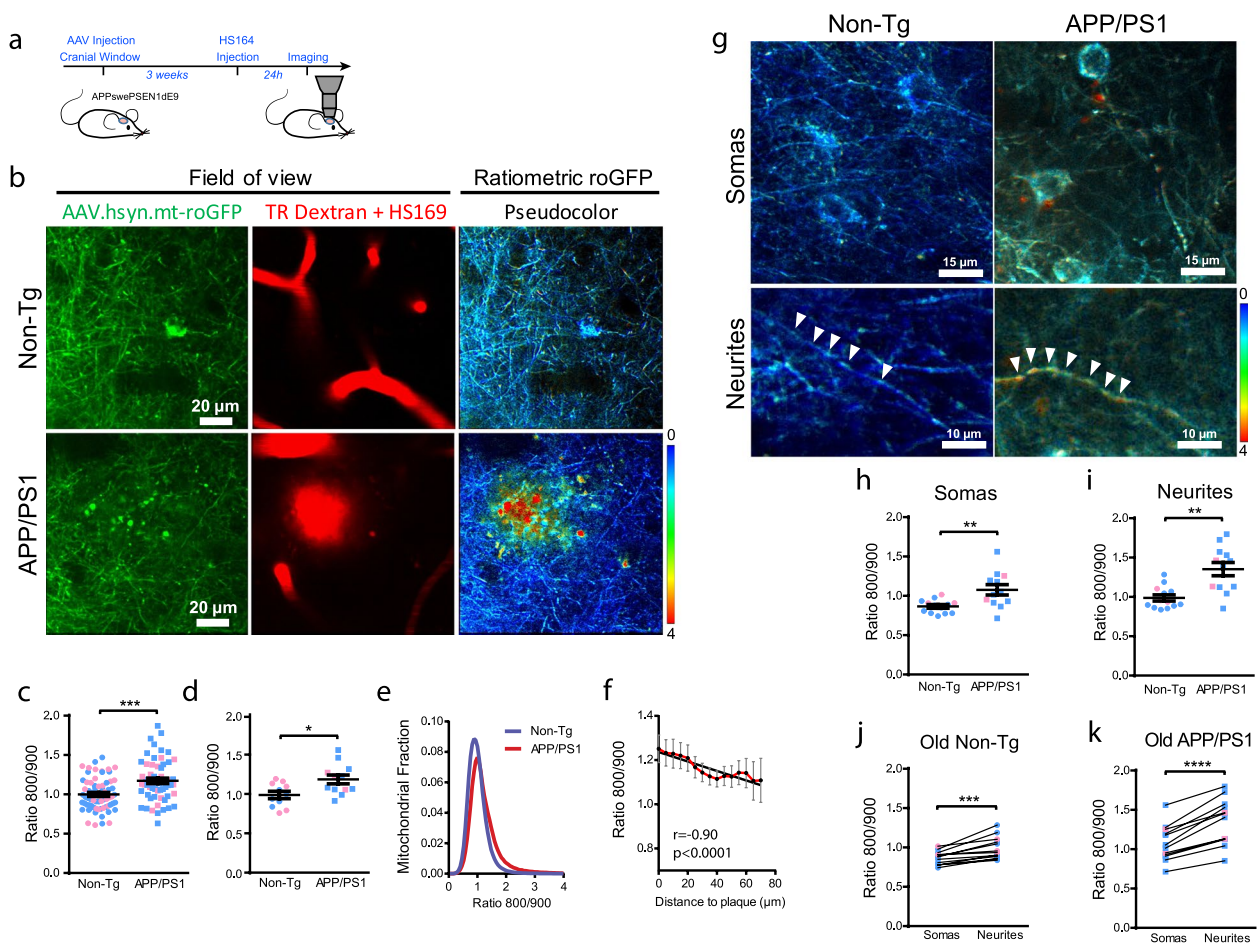


Fig. 2 Mitochondrial oxidative stress in AD transgenic mouse neurons after A β plaque deposition. **a** Experimental procedure to determine oxidative stress in neuronal mitochondria in mice. APP/PS1 Tg and non-Tg mice were injected with AAV.hSyn.mt-roGFP and a cranial window was implanted. Three weeks later, oxidative stress was assessed by two photon microscopy. Texas Red (TR) Dextran 70 kDa was used to create a fluorescent angiogram. HS169 was used to label A β plaques. **b** In vivo images of neurites and cell bodies expressing AAV.hSyn.mt-roGFP in mitochondria in non-Tg (top) and APP/PS1 Tg mice (bottom). Field of view shows two-photon images of the expression of the AAV (green), blood vessels (Dextran, red) and A β plaques (HS169, red) in the cortex. Ratiometric roGFP imaging shows pseudocolor images according to the pseudocolor scale on the bottom. Scale bar represents 20 μ m. **c, d** Mitochondrial oxidative stress (Ratio 800/900) comparison between non-Tg and APP/PS1 Tg mice at 10 months of age (i.e., after plaque deposition) in neuronal mitochondria (**c**, average per field of view. non-Tg: 1.00 ± 0.024 , $n = 69$ z-stacks; APP/PS1: 1.17 ± 0.034 , $n = 60$ z-stacks from 11 and 12 mice respectively, $***p = 0.0001$. **d**, average per mouse. non-Tg: 0.99 ± 0.046 , $n = 11$ mice (5 males, 6 females); APP/PS1: 1.19 ± 0.056 , $n = 12$ mice (9 males, 3 females), $p = 0.0224$. Blue dots denote male and pink dots denote female). Error bars represent mean \pm SEM. **e** Histogram of mitochondrial oxidative stress frequency distribution (indicated by Ratio 800/900) in neurons in non-Tg (blue) and APP/PS1 Tg mice (red). **f** Within 70 μ m distance from the edge of a plaque, the probability of finding mitochondrial oxidative stress in neurons was higher the closer to the plaque (mean \pm SEM; r (Pearson's correlation coefficient) -0.90 , R^2 0.81 , $****p < 0.0001$, $n = 33$ plaques analysed from 8 Tg mice). **g** Representative high magnification pseudocolor images of somas (top) and neurites (bottom) expressing AAV.hSyn.mt-roGFP in mitochondria in vivo in non-Tg (left) and APP/PS1 Tg mice (right). Scale bars represent 15 or 10 μ m. **h, i** Comparison of mitochondrial oxidative stress (Ratio 800/900) in somas and neurites in 10-mo-old non-Tg and APP/PS1 Tg mice. APP/PS1 Tg mice showed significantly higher oxidative stress levels in mitochondria in both compartments. Error bars represent mean \pm SEM (**h**, Neuronal somas: 0.87 ± 0.024 , $n = 13$ z-stacks from 4 non-Tg mice (3 males, 1 females), and 1.08 ± 0.067 , $n = 12$ z-stacks from 6 APP/PS1 Tg mice (4 males, 2 females). $**p = 0.006$. **i**, Neurites: 0.99 ± 0.039 , $n = 13$ z-stacks from 4 non-Tg mice (3 males, 1 females), and 1.35 ± 0.084 , $n = 12$ z-stacks from 6 APP/PS1 Tg mice (4 males, 2 females). $**p = 0.002$). **j, k** Comparison of mitochondrial oxidative stress (Ratio 800/900) in the different cell compartments (somas and neurites) in 10-month-old (old) non-Tg (**j**) and APP/PS1 Tg mice (**k**). Neurites showed significantly higher oxidative stress levels in mitochondria in both conditions. Error bars represent mean \pm SEM. (**j**, Old non-Tg: 0.87 ± 0.024 for somas and 0.99 ± 0.039 for neurites, $n = 13$ z-stacks from 4 mice (3 males, 1 females), $***p = 0.0003$. **k**, Old APP/PS1: 1.08 ± 0.065 for somas and 1.35 ± 0.084 for neurites, $n = 12$ z-stacks from 6 mice (4 males, 2 females), $****p < 0.0001$). Blue dots denote male and pink dots denote female

mitochondria, we also evaluated mice at 3 months of age, that is, prior to A β plaque deposition. The overall mitochondrial redox state did not significantly differ between young APP/PS1 Tg and non-Tg mice (Supplementary Fig. 6). Interestingly, however, we observed an increased mitochondrial oxidative stress in the neurites of young APP/PS1 Tg mice when compared to the non-Tg mice, suggesting that the small amount of soluble A β already present in the brain of these mice [36] could have an effect in the more susceptible neurites at this younger age (Supplementary Fig. 6e, f). Additionally, the mitochondrial redox state was higher in neurites than in somas only in the APP/PS1 Tg mice at this age, whereas it did not differ between both compartments in the non-Tg mice (Supplementary Fig. 6g). Taken together, these data demonstrate that mitochondrial oxidation is increased in the APP/PS1 Tg mice once A β plaques have been deposited, and in some susceptible neurites before plaque deposition likely due to soluble A β .

Soluble A β oligomers contribute to the oxidative stress of neuronal mitochondria in vivo.

A β plaques are surrounded by a halo of soluble A β oligomers (A β o) [37], therefore we aimed to investigate how soluble A β o directly contribute to the oxidative stress insult in neuronal mitochondria observed in the APP/PS1 Tg mouse. To this end, we used a preparation of naturally secreted soluble A β o, previously characterized and shown to contain low molecular weight A β o [12, 38]. A β -enriched medium was obtained from primary neurons prepared from Tg2576 embryos (heretofore transgenic conditioned media, TgCM). As control conditions, we used conditioned media from Wt littermates (Wt conditioned media, WtCM) and A β -immunodepleted TgCM, which was obtained after immunoprecipitating A β from the TgCM to anti- β -amyloid monoclonal antibody (6E10, amino acids 1–16). For these experiments, C57Bl/6 J mice were injected with AAV.hSyn.mt-roGFP and, after stable expression of the AAV, the naïve brains were first imaged in baseline conditions (before). Then, either WtCM, TgCM, or A β -immunodepleted TgCM was topically applied onto the mouse brain, and the same cortical volumes were re-imaged (after), allowing for direct comparison of the Ratio 800/900 between both timepoints (Fig. 3a). Representative images of mitochondrial oxidative stress in neurons before and after CM exposure are shown in Fig. 3b (and Supplementary Fig. 7). We found that the mitochondrial redox state was increased only after application of TgCM, whereas WtCM and A β -immunodepleted TgCM (Fig. 3c-g) did not alter the Ratio 800/900. Changes were relatively small, but comparable to the changes observed in the adult APP/PS1 Tg mouse. Although only a small fraction of mitochondria is affected by A β aggregates, these results support a detrimental role of soluble A β o

existing around A β plaques in the increased mitochondrial redox state in vivo.

Inhibition of calcium influx into mitochondria prevents neurons from A β -induced mitochondrial oxidative stress.

An important role of mitochondrial calcium (Ca²⁺) overload in both oxidative stress-induced neuronal cell death and excitotoxicity has been proposed [39, 40]. Mitochondrial Ca²⁺ signaling stimulates oxidative phosphorylation (OXPHOS) and ATP synthesis [41]. However, excessive entry of Ca²⁺ into mitochondrial matrix (i.e., mitochondrial Ca²⁺ overload) causes detrimental effects, including mitochondrial membrane potential loss, OXPHOS uncoupling, mitochondrial permeability transition pore opening and eventual cell death [42, 43]. Additionally, we have previously demonstrated that there is an A β -induced mitochondrial Ca²⁺ overload in neurons from APP/PS1 Tg mice, as well as after application of soluble A β o onto the Wt naïve brain [8], and that there is a close temporal link between mitochondrial Ca²⁺ overload and the rare neuronal cell death events occurring in these mice [8, 44]. Here we investigated whether the A β -driven changes in mitochondrial redox levels shown above are mediated via increased mitochondrial Ca²⁺ influx into the mitochondrial matrix. The mitochondrial calcium uniporter (MCU) is the main entrance of Ca²⁺ into mitochondria [45, 46]. Following the same experimental protocol as in Fig. 3a, we found that blockage of the mitochondrial Ca²⁺ uniporter with the specific cell-permeable MCU inhibitor Ru360 [47] (100 μ M) prevented overproduction of mitochondrial ROS, measured as the Ratio 800/900, upon application of TgCM onto the Wt mouse brain (Fig. 4). Figure 4a (and Supplementary Fig. 8) show representative images of mitochondria in baseline conditions (before) and after treatment with TgCM (after) in the presence or absence of Ru360, and with Ru360 alone. Since pretreatment with Ru360 abrogated the A β o-induced increase in mitochondrial oxidation (Fig. 4b-f), these findings indicate that increased mitochondrial oxidative stress levels are downstream mitochondrial Ca²⁺ overload and that pharmacological inhibition of MCU exerts a neuroprotective effect on A β -induced mitochondrial oxidative stress.

A β -associated mitochondrial oxidative stress is reduced with the mitochondrial-targeted antioxidant SS31 in AD transgenic mouse neurons.

To further assess the value of mitochondrial oxidative stress as a therapeutic target, we next evaluated the efficacy of SS31, a mitochondria-targeted antioxidant [48, 49], to reduce the mitochondrial oxidative stress levels in APP/PS1 Tg mice. Elamipretide (SS31, D-Arg-Dmt-Lys-Phe-NH₂) peptide [48, 49], is a mitochondria targeted antioxidant reported to eliminate ROS and

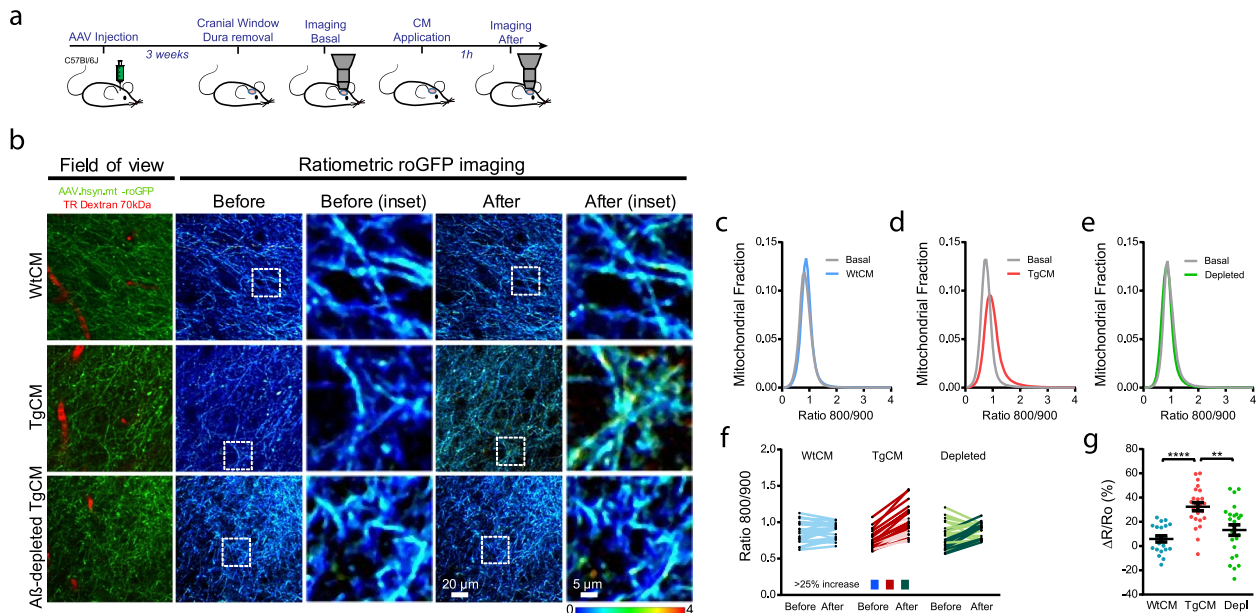


Fig. 3 Soluble A β oligomers increase oxidative stress in mitochondria in neurons in vivo. **a** Experimental procedure to determine the effects of A β on mitochondrial oxidative stress in the healthy mouse brain in vivo. 4-mo-old C57Bl/6 mice were injected with AAV.hSyn.mt-roGFP and a cranial window was implanted 3 weeks later. Oxidative stress in mitochondria was assessed by two photon microscopy in basal conditions and after topical application of either WtCM, TgCM or A β -immunodepleted TgCM. **b** Representative pictures of the effects of CM in neuronal mitochondria in the Wt mouse brain. Scale bar represents 20 μ m and 5 μ m in the insets. Only TgCM was able to increase oxidative stress levels. **c—e** Graphs show histograms of mitochondrial oxidative stress frequency distribution (Ratio 800/900) for the three conditions before (basal) and after application of CM in neurons. **f** Averaged 800/900 ratios before and after CM treatment for each z-stack acquired. Darker traces represent z-stacks showing an increase $\geq 25\%$ in Ratio 800/900 after topical application of CM. **g** Scatter dot plot represents the relative change ($\Delta R/R_o$) in ratio for each condition. Error bars represent mean \pm SEM (WtCM: $5.90 \pm 2.534\%$, $n = 21$ z-stacks; TgCM: $32.50 \pm 3.328\%$, 24 z-stacks; depleted TgCM: $13.20 \pm 4.340\%$, 24 z-stacks from 4, 4 and 5 mice respectively (all male), $**p < 0.01$, $****p < 0.0001$)

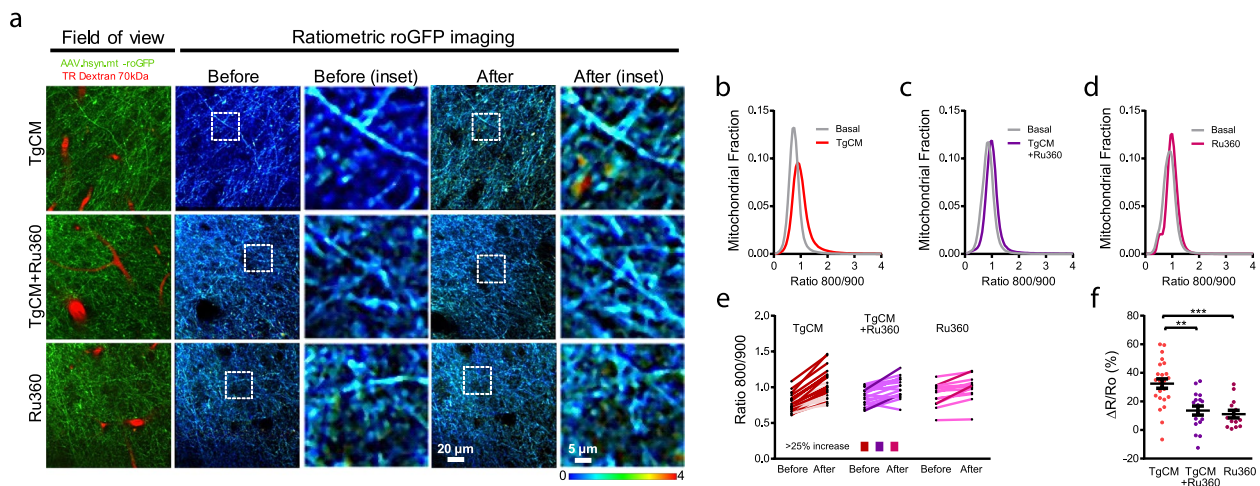


Fig. 4 Inhibition of the MCU prevents neurons from mitochondrial oxidative stress. **a** Representative pictures of the effects of the inhibition of the MCU on the mitochondrial oxidative stress induced by TgCM in neurons. Scale bar represents 20 μ m and 5 μ m in the insets. After exposure to Ru360, TgCM not was able to increase oxidative stress in mitochondria. **b—d** Histograms of mitochondrial oxidative stress frequency distribution (Ratio 800/900) before and after application of TgCM with or without Ru360, and of Ru360 alone. **e** Averaged Ratios 800/900 before and after TgCM treatment with or without Ru360, and Ru360 alone for each z-stack acquired. Darker traces represent z-stacks showing an increase $\geq 25\%$ in 800/900 ratio after topical application of TgCM or Ru360. **f** Scatter dot plot shows the relative change ($\Delta R/R_o$) in ratio 800/900 for each condition. Error bars represent mean \pm SEM (TgCM: $32.50 \pm 3.328\%$, 24 z-stack; TgCM + Ru360: $13.64 \pm 3.187\%$, 17 z-stacks; Ru360: $11.14 \pm 2.660\%$, 14 z-stacks from 4, 4 and 3 mice respectively (all male), $**p < 0.01$, $****p < 0.001$)

increase ATP production in mitochondria, thus maintaining the mitochondrial membrane potential, and preventing the opening of the mitochondrial permeability transition pore, mitochondrial swelling and cytochrome c release leading to apoptosis [50]. SS31 is currently being tested at the preclinical stage as a promising drug against neurodegenerative diseases, inflammatory diseases, and ischemia–reperfusion injury [10, 51–56].

APP/PS1 Tg mice and non-Tg controls were intraperitoneally injected for 8 weeks with 5 mg/kg SS31, starting at 8 months of age (Fig. 5a and Supplementary Fig. 9). We used SS20, another SS tetra-peptide which lacks the free radical scavenging properties, as control

[48]. AAV.hSyn.mt-roGFP was intracortically injected, and mitochondrial redox levels in neurons were evaluated when mice were 10-month-old. Treatment with SS31 in APP/PS1 Tg mice led to a significant decrease in the relative mitochondrial oxidative stress (Ratio 800/900) relative to SS20-treated APP/PS1 Tg mice, and down to the levels of non-Tg mice treated with SS31 (Fig. 5). The effect of SS31 was more efficacious in female APP/PS1 Tg (Fig. 5f). Additionally, the statistically significant association between oxidative stress levels and the proximity to A β plaques was lost in SS31-treated APP/PS1 Tg mice (Fig. 5g), as compared to the SS20-treated APP/PS1 Tg mice. These findings show that

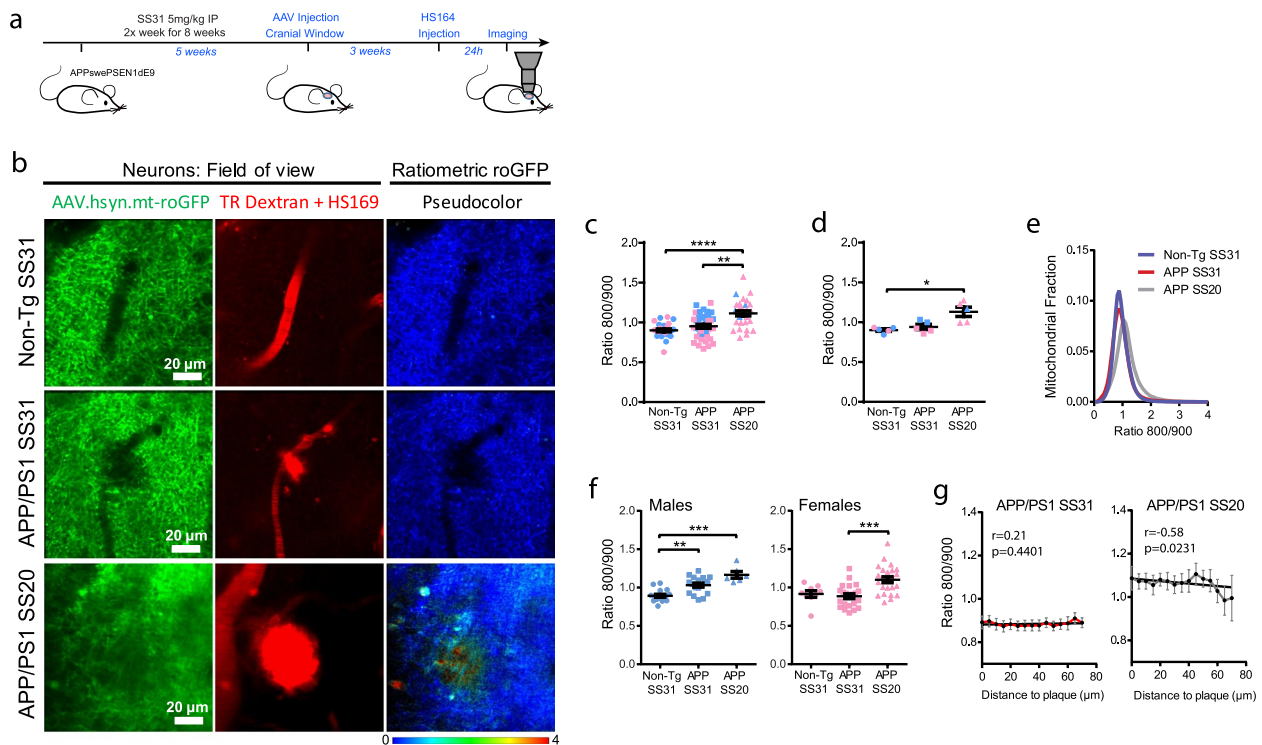


Fig. 5 The antioxidant targeted to mitochondria SS31 reduces mitochondrial oxidative stress in AD transgenic mouse neurons. **a.** Experimental procedure to determine oxidative stress in neuronal mitochondria in mice. **b.** In vivo images of neurites and cell bodies expressing AAV.hSyn.mt-roGFP in mitochondria in non-Tg (top) and APP/PS1 Tg mice treated with either SS31 (middle) or SS20 (bottom). Field of view shows two-photon images of the expression of the AAV (green), blood vessels (Dextran, red) and amyloid plaques (HS169, red) in the cortex. Ratiometric roGFP imaging shows pseudocolor images according to the pseudocolor scale at the bottom. Scale bar represents 20 μ m. **c, d.** Mitochondrial oxidative stress (Ratio 800/900) comparison between non-Tg and APP/PS1 Tg mice injected with either SS31 or SS20 in neuronal mitochondria (**c.** Average per field of view, non-Tg SS31: 0.94 ± 0.023 , $n = 32$ z-stacks from 6 mice (4 males, 2 females); APP/PS1 SS31: 0.95 ± 0.024 , $n = 40$ z-stacks from 6 mice (3 males, 3 females); APP/PS1 SS20: 1.11 ± 0.032 , $n = 30$ z-stacks from 5 mice (1 male, 4 females), $***p = 0.0001$, $**p < 0.01$. **d.** Average per mouse, non-Tg SS31: 0.90 ± 0.016 , $n = 6$ mice (4 males, 2 females); APP/PS1 SS31: 0.94 ± 0.032 , $n = 6$ mice (3 males, 3 females); APP/PS1 SS20: 1.13 ± 0.058 , $n = 5$ mice (1 male, 4 females), $*p < 0.05$). Error bars represent mean \pm SEM. Blue dots denote male and pink dots denote female. **e.** Histogram of mitochondrial oxidative stress frequency distribution (Ratio 800/900) of the three conditions. **f.** Difference between males and females (per field of view): Males non-Tg SS31: 0.89 ± 0.019 , $n = 17$ z-stacks; APP/PS1 SS31: 1.03 ± 0.026 , $n = 18$ z-stacks; APP/PS1 SS20: 1.17 ± 0.043 , $n = 8$ z-stacks from 4, 3 and 1 mice respectively, $**p = 0.01$, $***p = 0.001$; Females non-Tg SS31: 0.91 ± 0.042 , $n = 9$ z-stacks; APP/PS1 SS31: 0.87 ± 0.032 , $n = 22$ z-stacks; APP/PS1 SS20: 1.10 ± 0.038 , $n = 24$ z-stacks from 2, 3 and 4 mice respectively, $***p = 0.001$. **g.** For APP/PS1 Tg mice injected with SS31, the probability of finding mitochondrial oxidative stress in neurons was similar at any distance within 70 μ m from the edge of a plaque, unlike SS20 (mean \pm SEM; APP/PS1 SS31 r (Pearson's coefficient) 0.21, R^2 0.046, n.s., $n = 56$ plaques from 6 Tg mice; APP/PS1 SS20 $r = -0.58$, R^2 0.338, $*p < 0.05$, $n = 19$ plaques analysed from 4 Tg mice)

SS31 modifies mitochondrial redox state and ameliorates A β -related toxicity in neuronal mitochondria.

To determine whether SS31 reduces A β plaque burden, we quantified the extent of A β deposition in the cortex of SS31- and SS20-treated APP/PS1 Tg mice *ex vivo*. Conventional anti-A β immunolabeling detecting all A β deposits (diffuse and dense-core plaques) and ThioS staining (detecting the dense-core of plaques) revealed that neither the A β area fraction nor the density of A β deposits was significantly different between SS31- and SS20-treated APP/PS1 Tg mice (Supplementary Fig. 10a, b). Mitochondria are highly impaired in the dystrophic neurites that surround A β plaques [57, 58] and dystrophic neurites exhibit high levels of oxidation, especially surrounding A β plaques ([16]). To further evaluate the protective effects of SS31 in the A β plaque microenvironment, we analyzed the density of neuritic dystrophies per plaque [38, 59, 60]. Numerous abnormal neurites were generally associated with A β plaques in SS20-treated APP/PS1 Tg mice, but the total amount of dystrophies as well as the percentage of plaques showing dystrophies were reduced in Tg mice treated with SS31 (Supplementary Fig. 10c-e). Taken together, these results show that SS31 has a dramatic beneficial impact on an array of A β -associated neurotoxic events in the vicinity of A β plaques without altering A β plaque burden.

Human brain RNA-seq shows a downregulation of neuronal mitochondrial antioxidant capacity in AD

Finally, we evaluated the mitochondrial antioxidant defense capacity of neuronal mitochondria in the AD vs. the normal aging brain by interrogating a publicly available human single-nuclei RNA-seq dataset [17]. Specifically, we compared the expression of 31 genes encoding antioxidant mitochondrial proteins in various cell types across AD (Braak stages V/VI) and control (Braak stages 0/I/II) individuals. We observed that the expression of mitochondrial antioxidant defense genes was downregulated in neurons (both excitatory and inhibitory), with no changes observed in astrocytes and other cell types (oligodendrocytes and endothelial cells) (Fig. 6 and Supplemental Table 1). These results suggest that the expression of most human genes involved in the mitochondrial antioxidant defense of neurons is altered in AD patients at the transcriptional level.

Discussion

Previous *in vitro* and *in vivo* studies suggest that mitochondrial oxidative stress is related to AD pathology [61–65]. However, the sequence of pathogenic events and

whether the use of mitochondria-targeted antioxidant compounds can ameliorate this stress remained elusive, mainly because until recently it was not possible to investigate these questions *in vivo* in living mouse models. Here, we address these questions by using multiphoton microscopy in combination with cell type-specific redox analysis in a mouse model of cerebral β amyloidosis. The main findings of our *in vivo* study are as follows: (1) Mitochondrial oxidative stress is exacerbated in neurons in surrounding A β plaques; (2) soluble A β oligomers contribute to the increased mitochondrial oxidative stress levels; (3) A β -driven increased mitochondrial redox levels can be corrected by precluding mitochondrial Ca²⁺ influx into mitochondria via MCU inhibition; (4) the mitochondria targeted antioxidant SS31 (also known as Elamipretide) prevents A β -induced increased oxidative stress levels in neuronal mitochondria and ameliorates A β -plaque associated dystrophic neurites.

We found increased mitochondrial redox levels in neurons from the APP/PS1 Tg mice mostly after A β plaque deposition, and particularly close to plaques. Our group has previously shown that oxidative stress in the neuronal cytosol also occurs after plaque deposition in the APP/PS1 Tg mouse model [16], and our present findings suggest that this feature could be secondary to mitochondrial damage. When examining sex differences, the effect was greater for males, although females showed a tendency. This difference could be explained by an increased baseline mitochondrial redox levels in the non-Tg females, although further studies are needed to understand the contribution of aging and sex to these results. Neurons are highly compartmentalized cells, and every compartment can have unique mitochondrial requirements [66]. Dendrites are usually more susceptible to oxidative insult [67], and damaged mitochondria are known to have reduced motility, minimizing the spread of oxidation throughout the neuron and especially the soma, possibly explaining these differences between neurites and somas. Alternatively, this finding could be related to an increased bioenergetic demand associated with buffering Ca²⁺ near a synapse [68]. Unfortunately, the hSyn promoter does not allow distinguishing between different neuronal populations, since it infects both excitatory and inhibitory neurons. The use of alternative promoters and/or Cre mice would allow targeting different neuronal populations, in order to understand their different susceptibility to mitochondrial oxidative stress. Interestingly, oxidative stress has been recently proposed as the pathological mechanism leading to parvalbumin expressing interneurons impairment in schizophrenia and some forms of autism [69]; and different neuronal activity has been observed between excitatory and subgroups

a

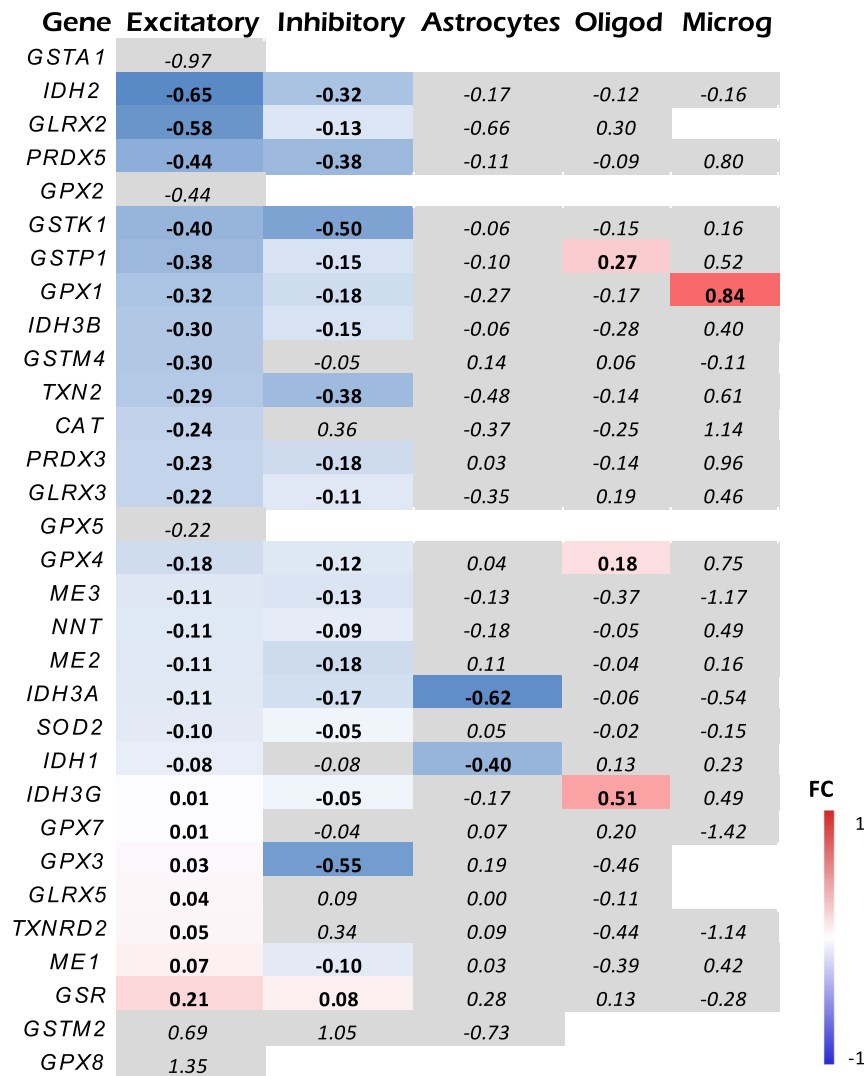


Fig. 6 Single cell RNA-seq shows a decrease in the mitochondrial antioxidant defense in neurons. **a.** Heat map representing fold change (FC) of the expression of genes encoding proteins involved in mitochondria antioxidant defense between AD (Braak NFT stages V/VI) and control individuals (Braak NFT stages 0/II) (from ref. [17]). The color of each box indicates the direction and magnitude of gene expression fold change. Grey color means statistically non-significant ($p > 0.05$) differences. Note that the expression of mitochondrial antioxidant defense genes is overall downregulated in both excitatory and inhibitory neurons, whereas no change is observed in astrocytes and other cell types. *CAT* (catalase), *GLRX* (glutaredoxin), *GPX* (glutathione peroxidase), *GSR* (glutathione reductase), *GST* (glutathione transferase), *IDH* (isocitrate dehydrogenase), *PRDX* (peroxiredoxins), *ME* (malic enzyme), *NNT* (nicotinamide nucleotide transhydrogenase), *SOD2* (manganese superoxide dismutase), *TXN2* (thioredoxin), *TXNRD* (thioredoxin reductase)

of inhibitory neurons in the APP/PS1 mouse model of AD [70]. This highlights the importance of understanding the different susceptibility of independent neuronal populations as specific targets for the treatment of neurodegenerative diseases, including AD, and opens follow up questions to the current study.

Mitochondrial oxidative stress levels correlated negatively with the proximity to A β plaques in the APP/PS1

Tg mice is consistent with our previous studies showing higher cytosolic oxidative stress levels [16] and cytosolic Ca²⁺ overload [71] in the immediate vicinity of individual plaques; however, we found mitochondrial Ca²⁺ overload to be independent of the distance to A β plaques [8]. Even though we can only speculate on this discrepancy, it is plausible that most of the elevated oxidative stress observed comes from damaged mitochondria

accumulating in dystrophic neurites around A β plaques, and whose mitochondrial antioxidant natural defense is compromised, whereas mitochondrial Ca²⁺ overload may be a more widespread phenomenon. In line with these results, our group has previously shown structurally and functionally damaged mitochondria around A β plaques [32]. These mitochondria are prone to produce more ROS and less ATP, likely contributing to neurodegenerative phenotypes observed in these mice such as dystrophic neurites and synaptic loss. Herein, a major focus of our study was to analyze the impact of acute oxidative insult induced by soluble A β within the neuronal mitochondria. We found that mitochondrial redox state levels were increased after application of soluble A β (TgCM) to the naïve Wt mouse brain, (vs. WtCM or A β -immunodepleted TgCM), implying that A β are also involved in the neuronal mitochondrial oxidative stress observed in AD. In line with these results, the concentration of soluble oligomeric A β increases with age in the APP/PS1 Tg mouse model [33, 36, 72], which could contribute to the increased redox level observed in the older Tg mice.

Increased neuronal activity enhances mitochondrial superoxide production via excessive cytosolic Ca²⁺ load [73–75], which could in turn lead to mitochondrial Ca²⁺ overload (since mitochondria buffer excessive cytosolic Ca²⁺) leading to neurotoxicity. We found that inhibition of MCU, the main route for Ca²⁺ influx into the mitochondria, via blocking its pore with the specific drug Ru360, attenuated the A β -driven mitochondrial oxidative stress. This finding places mitochondrial Ca²⁺ dys-homeostasis upstream oxidative stress and deciphers the most likely sequence of events in vivo. While dysregulation in mitochondrial Ca²⁺ signaling and increased ROS production have been observed separately in various in vitro models and a *C. elegans* model of AD [76], here we have demonstrated a link between both deleterious events in vivo in a mouse model of AD. Future work will determine whether A β drives a vicious cycle in which mitochondrial Ca²⁺ overload leads to mitochondrial oxidative stress and whether this exacerbates mitochondrial Ca²⁺ overload, since a better understanding of the links between mitochondrial Ca²⁺, MCU, and oxidative stress could propel the development of mitoprotective therapies against AD and perhaps other neurodegenerative diseases.

Neurons need to maintain mitochondrial function even after a local insult and, to accomplish this, the cells use mitochondrial antioxidants which protect against the ensuing toxicity. Severely damaged mitochondria decrease their antioxidant defense, thus increasing ROS production. In line with this concept, we observed a downregulation of the expression of the mitochondrial

antioxidant defense genes in neurons from AD brains by interrogating a public snRNA-seq dataset. Additionally, the mitochondrial antioxidant defense could be impaired in the setting of mitochondrial Ca²⁺ overload due to the direct inhibition of the antioxidant enzymes by the high Ca²⁺ levels [77].

Using the hSyn.mt-roGFP sensor and multiphoton microscopy, we also found relative reduced mitochondrial oxidative stress in neurons in the SS31-treated APP/PS1 Tg mice, compared to SS20-treated ones. Therapeutic clinical trials with natural antioxidants have generally shown mixed results. Some prevention trials have shown that treatment of elderly people with vitamins C and E reduces the risk of AD [78–80], whereas others did not [81–84]. It has been proposed that these hydrosoluble vitamins are not able to cross the blood brain barrier and reach brain cells. SS31 is a cell permeable small peptide that can easily penetrate in neurons and concentrate in the mitochondrial matrix [85]. SS31 has been shown to delay the progression of behavioral deficits in APP/PS1 treated mice [86]; and to protect against Ca²⁺-induced mitochondrial depolarization and swelling, and several mitochondrial insults, including A β toxicity, in treated N2a cells and primary neurons from Tg mice [87]. While another study reported that SS31 reduces soluble A β levels and A β deposits in APP Tg mice, leading to an improvement in mitochondrial function [11], we did not detect significant changes in A β plaque burden, whether measured by area fraction (% immunoreactive area) or density (number/mm²) of total or dense-core (ThioS-positive) plaques. Instead, the number of dystrophic neurites per plaque was significantly reduced upon SS31 treatment, suggesting that mitochondrial oxidative stress contributes to this neurodegenerative feature of A β plaques [88]. This finding is particularly intriguing because A β plaque-associated dystrophic neurites are known to accumulate damaged mitochondria [58, 89]. In addition, a reduction in plaque-associated dystrophic neurites may have a clinical correlate because they are thought to accumulate over the clinical course of AD [90] and impact network functioning [91, 92]. While observational studies with dietary or supplemented antioxidants have showed benefits in AD [93] or mild cognitive impairment [94], clinical trials testing antioxidants have been generally unsuccessful against AD progression [95–97], and therefore there is a lot of skepticism about the success of the use of antioxidants as a therapy for AD. Some proposed reasons for the failure of antioxidants in clinical trials include low permeability of the blood brain barrier to antioxidants, therapeutic dosage, poor study design or timing at which the antioxidant should be provided during the progression of the disease [98]. Our study is the first to show in vivo in living mice that reducing mitochondrial ROS by treatment with

a mitochondria targeted antioxidant drug can ameliorate plaque-associated neuronal mitochondrial oxidative stress and dystrophic neurites without removing pathology, and therefore, could have therapeutic value in combination with anti-A β and anti-tau therapies.

Conclusion

Taken together, our findings expand the current knowledge about mitochondrial redox homeostasis in neurons and its impairment in AD. This is the first direct *in vivo* demonstration of exacerbated mitochondrial oxidative stress levels in the presence of A β aggregates in neurons, which we have shown by combining a mitochondrial redox reporter and intravital multiphoton microscopy. Even though a change in the mt-roGFP ratio does not mandate ROS generation in mitochondria (since ROS could be also generated in the cytosol and diffuse later into mitochondria), this sensor is an invaluable tool to measure the relative mitochondrial oxidative stress regardless of its source. We have also provided evidence that mitochondria-targeted antioxidants can ameliorate neuronal mitochondrial A β -induced oxidative stress, and A β -plaque-associated dystrophic neurites and, in combination with other therapies, might represent a novel strategy with potential therapeutic and/or preventative value in AD.

Abbreviations

AAV	Adeno-associated virus
AD	Alzheimer's disease
A β	Amyloid beta
CM	Conditioned media
DTDP	Dithiodipyridine
DTT	Dithiothreitol
MCU	Mitochondrial calcium uniporter
mt-roGFP	Matrix-roGFP
ROS	Reactive oxygen species
SS31	Elamipretide
Tg	Transgenic
Wt	Wild-type

Supplementary Information

The online version contains supplementary material available at <https://doi.org/10.1186/s13024-024-00702-2>.

Additional file 1: Fig. S1. Validation of AAV.hSyn.mt-roGFP *in vitro*. a. Mitochondrial co-transfection verified proper targeting of mt-roGFP to mitochondria. N2a cells (top) and primary cortical neurons (bottom) were co-transfected with mt-roGFP (green) and mRuby-Mito-7 (red) and subjected to confocal microscopy imaging. Scale bar represents 10 μ m. b. Double immunolabelling of mt-roGFP (green) and mRuby-ER5 (red, targeting endoplasmic reticulum, ER) in N2a cells shows lack of colocalization and supports the mitochondrial localization of mt-roGFP. Scale bar represents 10 μ m. c. *In vitro* imaging of cellular oxidative stress with mt-roGFP. Primary cortical neurons were exposed to either the oxidant DTDP or the reducing agent DTT. Images at 800 nm (red), 900 nm (green) and merged are shown. d. The relative changes in ratio 800/900 were represented by histograms of ratio 800/900 frequency distribution in control conditions (grey) and 20 min after exposure to DTT 1 mM (blue) and DTDP 100 μ M (red)

(Control, n = 143 cells; DTT 1 mM, n = 125; DTDP 100 μ M, n = 109 cells).

Fig. S2. Validation of pAAV.hSyn.mt-roGFP *ex vivo*. AAV.hSyn.mt-roGFP targets neuronal mitochondria *in vivo*. a. Colocalization of AAV.hSyn.mt-roGFP (green), NeuN (red) and GS (glutamine synthetase, magenta) in the mouse cortex shown by immunohistochemistry. Note that AAV.hSyn.mt-roGFP only colocalizes with the neuronal marker NeuN. Scale bar represents 10 μ m. b. Colocalization of AAV.hSyn.mt-roGFP (green), HSP60 (mitochondrial marker, red) and NeuN (magenta) in the cortex shown by immunohistochemistry. Scale bar represents 10 μ m. c. Inset. Colocalization of AAV.hSyn.mt-roGFP (green) and HSP60 (red) in cortex shown by immunohistochemistry (top). Scale bar 5 μ m. Graph shows intensity profile of the ROI across the cell. Green line represents the fluorescence intensity of AAV.hSyn.mt-roGFP and red line represents the fluorescence intensity of HSP60. **Fig. S3.** Original images excited at 800nm and 900nm of Fig. 1b. **Fig. S4.** Original images excited at 800nm and 900nm of Fig. 2b. **Fig. S5.** Mitochondrial oxidative stress in male and female mice. Mitochondrial oxidative stress (Ratio 800/900) in neurons was compared between non-Tg and APP/PS1 Tg mice at 10 months of age within males (a) or females (b). Note that only for males the difference is significantly different (a. Males: average per field of view: non-Tg: 0.95 ± 0.026 , n = 31 z-stacks; APP/PS1: 1.17 ± 0.046 , n = 41 z-stacks from 5 and 9 mice respectively, ****p = 0.0001; Average per mouse: non-Tg: 0.95 ± 0.037 , n = 5 mice; APP/PS1: 1.19 ± 0.073 , n = 9 mice, *p=0.0190. b. Females: average per field of view: non-Tg: 1.038 ± 0.038 , n = 38 z-stacks; APP/PS1: 1.17 ± 0.043 , n = 19 z-stacks from 6 and 3 mice respectively; Average per mouse: non-Tg: 1.02 ± 0.08 , n = 6 mice; APP/PS1: 1.19 ± 0.067 , n = 3 mice). Error bars represent mean \pm SEM. **Fig. S6.** The overall mitochondrial redox levels are not elevated in AD transgenic mouse neurons before A β plaque deposition. a. *In vivo* images of neurites and cell bodies expressing pAAV.hSyn.mt-roGFP in mitochondria in non-Tg (top) and APP/PS1 Tg mice (bottom) in young mice. Scale bar represents 10 μ m. b, c. Scatter dot plot represents overall mitochondrial oxidative stress (Ratio 800/900) in non-Tg and APP/PS1 Tg mice at 3 months of age, before plaque deposition, in mitochondria in neurons (b, average per field of view, non-Tg: 0.83 ± 0.024 , n = 18 z-stacks from 3 mice (3 male); APP/PS1: 0.87 ± 0.024 , n = 42 z-stacks from 6 mice (3 male, 3 female); c. average per mouse, non-Tg: 0.82 ± 0.039 , n = 3 mice (3 male); APP/PS1: 0.87 ± 0.034 , n = 6 mice (3 male, 3 female)). Error bars represent mean \pm SEM. Blue dots denote male and pink dots denote female. d. Histogram of mitochondrial oxidative stress frequency distribution (indicated by Ratio 800/900) in the young non-Tg and APP/PS1 Tg mice. e. Representative high resolution pseudocolor images of somas (top) and neurites (bottom) expressing AAV.hSyn.mt-roGFP in mitochondria *in vivo* in young non-Tg (left) and APP/PS1 Tg mice (right). Scale bar represents 15 or 10 μ m. f. Comparison of mitochondrial oxidative stress (Ratio 800/900) within somas or neurites in 3-month-old non-Tg and APP/PS1 Tg mice. APP/PS1 Tg mice showed higher oxidative stress levels in mitochondria in neurites. Error bars represent mean \pm SEM. (somas: 0.79 ± 0.023 , n = 9 z-stacks from 3 non-Tg mice (3 male), and 0.75 ± 0.026 , n = 10 z-stacks from 3 APP/PS1 Tg mice (1 male, 2 females); neurites: 0.82 ± 0.040 , n = 9 z-stacks from 3 non-Tg mice (3 male), and 0.92 ± 0.030 , n = 10 z-stacks from 3 APP/PS1 Tg mice (1 male, 4 females); *p = 0.0467). g. Comparison of mitochondrial oxidative stress (Ratio 800/900) in the different cell compartments (somas and neurites) in 3-month-old (old) non-Tg and APP/PS1 Tg mice. Neurites showed significantly higher oxidative stress levels in mitochondria in the APP/PS1 Tg mouse when compared to the somas. Error bars represent mean \pm SEM. (Young non-Tg: 0.79 ± 0.023 for somas and 0.82 ± 0.040 for neurites, n = 9 z-stacks from 3 mice (3 male); Young APP/PS1: 0.75 ± 0.026 for somas and 0.92 ± 0.030 for neurites, n = 10 z-stacks from 3 mice (1 male, 2 female), ****p = 0.0003). Blue dots denote male and pink dots denote female. **Fig. S7.** Original images excited at 800nm and 900nm of Fig. 3b. **Fig. S8.** Original images excited at 800nm and 900nm of Fig. 4a. **Fig. S9.** Original images excited at 800nm and 900nm of Fig. 5a. **Fig. S10.** SS31 reduces A β -associated dystrophic neurite number but not amyloid burden in the AD transgenic mouse. a. Representative images of the global amount of amyloid in the cortex of SS31 and SS20 treated APP/PS1 mice at 10 mo of age after A β immunostaining. Scale bar represents 100 μ m. b. Scatter dot plots represent the quantification of amyloid load in the cortex after

anti-A β immunostaining or ThioS labeling. The number of dense-core plaques detected by ThioS (top) and the overall load of A β (bottom) was comparable among SS31 and SS20 APP/PS1 treated mice. $n = 7$ mice per condition. Histograms represent the dense core plaque (top) and diffuse amyloid deposit (bottom) size in both conditions. c. Representative images of neuritic dystrophies (arrow heads, neurofilaments in green) around amyloid plaques (blue) in APP/PS1 mouse after either SS31 or SS20 treatment. Scale bar 20 μ m. d. Scatter dot plot represents the quantification of the number of dystrophic neurites observed per plaque, $n = 362$ plaques from 4 SS31 APP/PS1 treated mice and $n = 295$ plaques from 4 SS20 APP/PS1 treated mice, $**p < 0.05$. e. Scatter dot plot represents the percentage of plaques showing dystrophic neurites, $n = 4 - 5$ areas per 4 mouse per condition, $*p = 0.022$.

Additional file 2: Supplemental Table 1. Analysis of neuronal mitochondrial antioxidant capacity in AD vs. normal aging brain. The expression levels for genes encoding antioxidant enzymes (CAT, GLRX, GPX, GSR, GST, IDH, PRDX, ME, NNT, SOD2, TXN2, and TXNRD) were compared between control (B1, Braak NFT stages 0/I/II) and AD (B3, Braak NFT stages V/VI) individuals of a publicly available human single-nuclei RNA-seq [44]. The average expression level for each gene and group are shown, together with the log fold change and the adjusted p-value of the individual gene models, and the z-scores and the p-values of the mixed models.

Acknowledgements

Authors acknowledge the Schepens Eye Research Institute Gene Transfer Vector Core for the AAV:hSyn.mt-roGFP vector production.

Authors' contributions

MCR designed experiments, collected and analyzed data, and wrote the original draft. EKK, ACS, and MVSM helped with immunohistochemistry and mouse brain injections. SSH wrote ImageJ and Matlab macros. SD analyzed snRNA-seq data. ZF performed cloning design. HS and KPRN provided LCOs. ASP provided intellectual input and feedback and edited the manuscript. BJB conceptualized the research, designed experiments, discussed data, edited the manuscript and secured funding. All authors read and approved the final manuscript.

Funding

This work was supported by NHR01AG0442603, NHR56AG060974 and NIH510RR025645 (BJB), the Swedish Research Council 2016–00748 (KPRN), the Alzheimer' Association AACF-17–524184 and NIH/NIA K08AG064039 (AS-P), the Tosteson & Fund for Medical Discovery postdoctoral fellowship and the BrightFocus Foundation A2019488F (MCR).

Availability of data and materials

The authors declare that all data supporting the findings of this study are available within the article and its Supplementary Information files or from the corresponding author upon reasonable request.

Declarations

Competing interests

The authors declare that the research was conducted in the absence of any commercial or financial relationships that could be construed as a potential conflict of interest.

Author details

¹Department of Neurology, Massachusetts General Hospital and Harvard Medical School, 114, 16Th St, Charlestown, MA 02129, USA. ²Department of Physics, Chemistry and Biology, Linköping University, 581 83 Linköping, Sweden. ³Present address: Foundational Neuroscience Center, AbbVie Inc, Cambridge, MA, USA.

Received: 3 June 2023 Accepted: 5 January 2024

Published online: 18 January 2024

References

- Budd Haeberlein S, Aisen PS, Barkhof F, Chalkias S, Chen T, Cohen S, et al. Two Randomized Phase 3 Studies of Aducanumab in Early Alzheimer's Disease. *J Prev Alzheimers Dis.* 2022;9(2):197–210.
- van Dyck CH, Swanson CJ, Aisen P, Bateman RJ, Chen C, Gee M, et al. Lecanemab in Early Alzheimer's Disease. *N Engl J Med.* 2023;388(1):9–21.
- Grimm A, Eckert A. Brain aging and neurodegeneration: from a mitochondrial point of view. *J Neurochem.* 2017;143(4):418–31.
- Kim TS, Pae CU, Yoon SJ, Jang WY, Lee NJ, Kim JJ, et al. Decreased plasma antioxidants in patients with Alzheimer's disease. *Int J Geriatr Psychiatry.* 2006;21(4):344–8.
- von Bernhardt R, Eugenin J. Alzheimer's disease: redox dysregulation as a common denominator for diverse pathogenic mechanisms. *Antioxid Redox Signal.* 2012;16(9):974–1031.
- Murphy MP, Smith RA. Targeting antioxidants to mitochondria by conjugation to lipophilic cations. *Annu Rev Pharmacol Toxicol.* 2007;47:629–56.
- Szeto HH. Mitochondria-targeted peptide antioxidants: novel neuroprotective agents. *AAPS J.* 2006;8(3):E521–31.
- Calvo-Rodriguez M, Hou SS, Snyder AC, Kharitonova EK, Russ AN, Das S, et al. Increased mitochondrial calcium levels associated with neuronal death in a mouse model of Alzheimer's disease. *Nat Commun.* 2020;11(1):2146.
- Waypa GB, Marks JD, Guzy R, Mungai PT, Schriewer J, Dokic D, et al. Hypoxia triggers subcellular compartmental redox signaling in vascular smooth muscle cells. *Circ Res.* 2010;106(3):526–35.
- Petri S, Kiaei M, Damiano M, Hiller A, Wille E, Manfredi G, et al. Cell-permeable peptide antioxidants as a novel therapeutic approach in a mouse model of amyotrophic lateral sclerosis. *J Neurochem.* 2006;98(4):1141–8.
- Reddy PH, Manczak M, Kandimalla R. Mitochondria-targeted small molecule SS31: a potential candidate for the treatment of Alzheimer's disease. *Hum Mol Genet.* 2017;26(8):1483–96.
- Arbel-Ornath M, Hudry E, Boivin JR, Hashimoto T, Takeda S, Kuchibhotla KV, et al. Soluble oligomeric amyloid-beta induces calcium dyshomeostasis that precedes synapse loss in the living mouse brain. *Mol Neurodegener.* 2017;12(1):27.
- Cannon MB, Remington SJ. Redox-sensitive green fluorescent protein: probes for dynamic intracellular redox responses. A review *Methods Mol Biol.* 2008;476:51–65.
- Calvo-Rodriguez M, Hou SS, Snyder AC, Dujardin S, Shirani H, Nilsson KPR, et al. In vivo detection of tau fibrils and amyloid beta aggregates with luminescent conjugated oligothiophenes and multiphoton microscopy. *Acta Neuropathol Commun.* 2019;7(1):171.
- Morgan B, Sobotta MC, Dick TP. Measuring E(GSH) and H2O2 with roGFP2-based redox probes. *Free Radic Biol Med.* 2011;51(11):1943–51.
- Xie H, Hou S, Jiang J, Sekutowicz M, Kelly J, Bacskaï BJ. Rapid cell death is preceded by amyloid plaque-mediated oxidative stress. *Proc Natl Acad Sci U S A.* 2013;110(19):7904–9.
- Mathys H, Davila-Velderrain J, Peng Z, Gao F, Mohammadi S, Young JZ, et al. Single-cell transcriptomic analysis of Alzheimer's disease. *Nature.* 2019;570(7761):332–7.
- Braak H, Braak E. Neuropathological staging of Alzheimer-related changes. *Acta Neuropathol.* 1991;82(4):239–59.
- Hochberg YBaY. Controlling the false discovery rate: a practical and powerful approach to multiple testing. *J Roy Statist Soc Ser B.* 57(1):289–300.
- Teixeira RB, Karbasiafshar C, Sabra M, Abid MR. Optimization of mito-roGFP protocol to measure mitochondrial oxidative status in human coronary artery endothelial cells. *STAR Protoc.* 2021;2(3):100753.
- Gao L, Arias-Mayenco I, Ortega-Saenz P, Lopez-Barneo J. Using redox-sensitive fluorescent probes to record real-time reactive oxygen species production in cells from mouse carotid body slices. *STAR Protoc.* 2021;2(2):100535.
- Dooley CT, Dore TM, Hanson GT, Jackson WC, Remington SJ, Tsien RY. Imaging dynamic redox changes in mammalian cells with green fluorescent protein indicators. *J Biol Chem.* 2004;279(21):22284–93.
- Hanson GT, Aggeler R, Oglesbee D, Cannon M, Capaldi RA, Tsien RY, et al. Investigating mitochondrial redox potential with redox-sensitive green fluorescent protein indicators. *J Biol Chem.* 2004;279(13):13044–53.
- Meyer AJ, Brach T, Marty L, Kreye S, Rouhier N, Jacquot JP, et al. Redox-sensitive GFP in *Arabidopsis thaliana* is a quantitative biosensor for the redox potential of the cellular glutathione redox buffer. *Plant J.* 2007;52(5):973–86.

25. Funke F, Gerich FJ, Muller M. Dynamic, semi-quantitative imaging of intracellular ROS levels and redox status in rat hippocampal neurons. *Neuroimage*. 2011;54(4):2590–602.
26. Grosser E, Hirt U, Janc OA, Menzfeld C, Fischer M, Kempkes B, et al. Oxidative burden and mitochondrial dysfunction in a mouse model of Rett syndrome. *Neurobiol Dis*. 2012;48(1):102–14.
27. Belousov VV, Fradkov AF, Lukyanov KA, Staroverov DB, Shakhbazov KS, Tersikh AV, et al. Genetically encoded fluorescent indicator for intracellular hydrogen peroxide. *Nat Methods*. 2006;3(4):281–6.
28. Weller J, Kizina KM, Can K, Bao G, Muller M. Response properties of the genetically encoded optical H₂O₂ sensor HyPer. *Free Radic Biol Med*. 2014;76:227–41.
29. Wiesman AI, Murman DL, May PE, Schantell M, Wolfson SL, Johnson CM, et al. Visuospatial alpha and gamma oscillations scale with the severity of cognitive dysfunction in patients on the Alzheimer's disease spectrum. *Alzheimers Res Ther*. 2021;13(1):139.
30. Stephen JM, Montano R, Donahue CH, Adair JC, Knoefel J, Qualls C, et al. Somatosensory responses in normal aging, mild cognitive impairment, and Alzheimer's disease. *J Neural Transm (Vienna)*. 2010;117(2):217–25.
31. Koch J, Hickey GA, Kajdasz ST, Hyman BT, Bacskai BJ. In vivo imaging of amyloid-beta deposits in mouse brain with multiphoton microscopy. *Methods Mol Biol*. 2005;299:349–63.
32. Xie H, Guan J, Borrelli LA, Xu J, Serrano-Pozo A, Bacskai BJ. Mitochondrial alterations near amyloid plaques in an Alzheimer's disease mouse model. *J Neurosci*. 2013;33(43):17042–51.
33. Garcia-Alloza M, Robbins EM, Zhang-Nunes SX, Purcell SM, Betensky RA, Raju S, et al. Characterization of amyloid deposition in the APP^{swe}/PS1^{dE9} mouse model of Alzheimer disease. *Neurobiol Dis*. 2006;24(3):516–24.
34. Eckert A, Hauptmann S, Scherping I, Rhein V, Muller-Spahn F, Gotz J, et al. Soluble beta-amyloid leads to mitochondrial defects in amyloid precursor protein and tau transgenic mice. *Neurodegener Dis*. 2008;5(3–4):157–9.
35. Harris JJ, Jolivet R, Attwell D. Synaptic energy use and supply. *Neuron*. 2012;75(5):762–77.
36. Takeda S, Hashimoto T, Roe AD, Hori Y, Spires-Jones TL, Hyman BT. Brain interstitial oligomeric amyloid beta increases with age and is resistant to clearance from brain in a mouse model of Alzheimer's disease. *FASEB J*. 2013;27(8):3239–48.
37. Koffie RM, Meyer-Luehmann M, Hashimoto T, Adams KW, Mielke ML, Garcia-Alloza M, et al. Oligomeric amyloid beta associates with postsynaptic densities and correlates with excitatory synapse loss near senile plaques. *Proc Natl Acad Sci U S A*. 2009;106(10):4012–7.
38. Wu HY, Hudry E, Hashimoto T, Kuchibhotla K, Rozkalne A, Fan Z, et al. Amyloid beta induces the morphological neurodegenerative triad of spine loss, dendritic simplification, and neuritic dystrophies through calcineurin activation. *J Neurosci*. 2010;30(7):2636–49.
39. Peng TI, Jou MJ. Oxidative stress caused by mitochondrial calcium overload. *Ann N Y Acad Sci*. 2010;1201:183–8.
40. Depp C, Bas-Orth C, Schroeder L, Hellwig A, Bading H. Synaptic Activity Protects Neurons Against Calcium-Mediated Oxidation and Contraction of Mitochondria During Excitotoxicity. *Antioxid Redox Signal*. 2018;29(12):1109–24.
41. Rizzuto R, De Stefani D, Raffaello A, Mammucari C. Mitochondria as sensors and regulators of calcium signalling. *Nat Rev Mol Cell Biol*. 2012;13(9):566–78.
42. Brookes PS, Yoon Y, Robotham JL, Anders MW, Sheu SS. Calcium, ATP, and ROS: a mitochondrial love-hate triangle. *Am J Physiol Cell Physiol*. 2004;287(4):C817–33.
43. Vercesi AE, Kowaltowski AJ, Grijalba MT, Meinicke AR, Castilho RF. The role of reactive oxygen species in mitochondrial permeability transition. *Biosci Rep*. 1997;17(1):43–52.
44. Calvo-Rodriguez M, Bacskai BJ. Mitochondria and Calcium in Alzheimer's Disease: From Cell Signaling to Neuronal Cell Death. *Trends Neurosci*. 2021;44(2):136–51.
45. De Stefani D, Raffaello A, Teardo E, Szabo I, Rizzuto R. A forty-kilodalton protein of the inner membrane is the mitochondrial calcium uniporter. *Nature*. 2011;476(7360):336–40.
46. Baughman JM, Perocchi F, Girgis HS, Plovanich M, Belcher-Timme CA, Sancak Y, et al. Integrative genomics identifies MCU as an essential component of the mitochondrial calcium uniporter. *Nature*. 2011;476(7360):341–5.
47. Kirichok Y, Krapivinsky G, Clapham DE. The mitochondrial calcium uniporter is a highly selective ion channel. *Nature*. 2004;427(6972):360–4.
48. Zhao K, Zhao GM, Wu D, Soong Y, Birk AV, Schiller PW, et al. Cell-permeable peptide antioxidants targeted to inner mitochondrial membrane inhibit mitochondrial swelling, oxidative cell death, and reperfusion injury. *J Biol Chem*. 2004;279(33):34682–90.
49. Birk AV, Chao WM, Bracken C, Warren JD, Szeto HH. Targeting mitochondrial cardiolipin and the cytochrome c/cardiolipin complex to promote electron transport and optimize mitochondrial ATP synthesis. *Br J Pharmacol*. 2014;171(8):2017–28.
50. Calkins MJ, Manczak M, Reddy PH. Mitochondria-Targeted Antioxidant SS31 Prevents Amyloid Beta-Induced Mitochondrial Abnormalities and Synaptic Degeneration in Alzheimer's Disease. *Pharmaceuticals (Basel)*. 2012;5(10):1103–19.
51. Zhao H, Li H, Hao S, Chen J, Wu J, Song C, et al. Peptide SS-31 upregulates frataxin expression and improves the quality of mitochondria: implications in the treatment of Friedreich ataxia. *Sci Rep*. 2017;7(1):9840.
52. Fetisova E, Chernyak B, Korshunova G, Muntyan M, Skulachev V. Mitochondria-targeted Antioxidants as a Prospective Therapeutic Strategy for Multiple Sclerosis. *Curr Med Chem*. 2017;24(19):2086–114.
53. Sabbah HN, Gupta RC, Kohli S, Wang M, Hachem S, Zhang K. Chronic Therapy With Elamipretide (MTP-131), a Novel Mitochondria-Targeting Peptide, Improves Left Ventricular and Mitochondrial Function in Dogs With Advanced Heart Failure. *Circ Heart Fail*. 2016;9(2):e002206.
54. Szeto HH, Liu S, Soong Y, Wu D, Darrah SF, Cheng FY, et al. Mitochondria-targeted peptide accelerates ATP recovery and reduces ischemic kidney injury. *J Am Soc Nephrol*. 2011;22(6):1041–52.
55. Siegel MP, Kruse SE, Percival JM, Goh J, White CC, Hopkins HC, et al. Mitochondrial-targeted peptide rapidly improves mitochondrial energetics and skeletal muscle performance in aged mice. *Aging Cell*. 2013;12(5):763–71.
56. Cai J, Jiang Y, Zhang M, Zhao H, Li H, Li K, et al. Protective effects of mitochondrion-targeted peptide SS-31 against hind limb ischemia-reperfusion injury. *J Physiol Biochem*. 2018;74(2):335–43.
57. Fiala JC, Feinberg M, Peters A, Barbas H. Mitochondrial degeneration in dystrophic neurites of senile plaques may lead to extracellular deposition of fine filaments. *Brain Struct Funct*. 2007;212(2):195–207.
58. Serrano-Pozo A, William CM, Ferrer I, Uro-Coste E, Delisle MB, Maurage CA, et al. Beneficial effect of human anti-amyloid-beta active immunization on neurite morphology and tau pathology. *Brain*. 2010;133(Pt 5):1312–27.
59. Garcia-Alloza M, Subramanian M, Thyssen D, Borrelli LA, Fauq A, Das P, et al. Existing plaques and neuritic abnormalities in APP:PS1 mice are not affected by administration of the gamma-secretase inhibitor LY-411575. *Mol Neurodegener*. 2009;4:19.
60. Fernandez-Martos CM, King AE, Atkinson RA, Woodhouse A, Vickers JC. Neurofilament light gene deletion exacerbates amyloid, dystrophic neurite, and synaptic pathology in the APP/PS1 transgenic model of Alzheimer's disease. *Neurobiol Aging*. 2015;36(10):2757–67.
61. Leuner K, Schutt T, Kurz C, Eckert SH, Schiller C, Occhipinti A, et al. Mitochondrion-derived reactive oxygen species lead to enhanced amyloid beta formation. *Antioxid Redox Signal*. 2012;16(12):1421–33.
62. Cheignon C, Tomas M, Bonnefont-Rousselot D, Faller P, Hureau C, Collin F. Oxidative stress and the amyloid beta peptide in Alzheimer's disease. *Redox Biol*. 2018;14:450–64.
63. Matsumura A, Emoto MC, Suzuki S, Iwahara N, Hisahara S, Kawamata J, et al. Evaluation of oxidative stress in the brain of a transgenic mouse model of Alzheimer disease by in vivo electron paramagnetic resonance imaging. *Free Radic Biol Med*. 2015;85:165–73.
64. Mao P, Manczak M, Calkins MJ, Truong Q, Reddy TP, Reddy AP, et al. Mitochondria-targeted catalase reduces abnormal APP processing, amyloid beta production and BACE1 in a mouse model of Alzheimer's disease: implications for neuroprotection and lifespan extension. *Hum Mol Genet*. 2012;21(13):2973–90.
65. Christopher Kwon YI, Xie W, Zhu H, Xie J, Shinn K, Juckel N, et al. gamma-Glutamyl-Transpeptidase-Resistant Glutathione Analog Attenuates Progression of Alzheimer's Disease-like Pathology and Neurodegeneration in a Mouse Model. *Antioxidants (Basel)*. 2021;10(11).
66. Misgeld T, Schwarz TL. Mitostasis in Neurons: Maintaining Mitochondria in an Extended Cellular Architecture. *Neuron*. 2017;96(3):651–66.

67. Grimm A, Cummins N, Gotz J. Local Oxidative Damage in the Soma and Dendrites Quarantines Neuronal Mitochondria at the Site of Insult. *iScience*. 2018;6:114–27.
68. Dryanovski DI, Guzman JN, Xie Z, Galteri DJ, Volpicelli-Daley LA, Lee VM, et al. Calcium entry and alpha-synuclein inclusions elevate dendritic mitochondrial oxidant stress in dopaminergic neurons. *J Neurosci*. 2013;33(24):10154–64.
69. Steullet P, Cabungcal JH, Coyle J, Didriksen M, Gill K, Grace AA, et al. Oxidative stress-driven parvalbumin interneuron impairment as a common mechanism in models of schizophrenia. *Mol Psychiatry*. 2017;22(7):936–43.
70. Algamal M, Russ AN, Miller MR, Hou SS, Maci M, Munting LP, et al. Reduced excitatory neuron activity and interneuron-type-specific deficits in a mouse model of Alzheimer's disease. *Commun Biol*. 2022;5(1):1323.
71. Kuchibhotla KV, Goldman ST, Lattarulo CR, Wu HY, Hyman BT, Bacskai BJ. Abeta plaques lead to aberrant regulation of calcium homeostasis in vivo resulting in structural and functional disruption of neuronal networks. *Neuron*. 2008;59(2):214–25.
72. Maia LF, Kaeser SA, Reichwald J, Hruscha M, Martus P, Staufenbiel M, et al. Changes in amyloid-beta and Tau in the cerebrospinal fluid of transgenic mice overexpressing amyloid precursor protein. *Sci Transl Med*. 2013;5(194):194re2.
73. Dykens JA. Isolated cerebral and cerebellar mitochondria produce free radicals when exposed to elevated Ca²⁺ and Na⁺: implications for neurodegeneration. *J Neurochem*. 1994;63(2):584–91.
74. Hongpaisan J, Winters CA, Andrews SB. Strong calcium entry activates mitochondrial superoxide generation, upregulating kinase signaling in hippocampal neurons. *J Neurosci*. 2004;24(48):10878–87.
75. Tretter L, Adam-Vizi V. High Ca²⁺ load promotes hydrogen peroxide generation via activation of alpha-glycerophosphate dehydrogenase in brain mitochondria. *Free Radic Biol Med*. 2012;53(11):2119–30.
76. Sarasija S, Laboy JT, Ashkavand Z, Bonner J, Tang Y, Norman KR. Presenilin mutations deregulate mitochondrial Ca(2+) homeostasis and metabolic activity causing neurodegeneration in *Caenorhabditis elegans*. *Elife*. 2018;7.
77. Zoccarato F, Cavallini L, Alexandre A. Respiration-dependent removal of exogenous H₂O₂ in brain mitochondria: inhibition by Ca²⁺. *J Biol Chem*. 2004;279(6):4166–74.
78. Morris MC, Evans DA, Bienias JL, Tangney CC, Bennett DA, Aggarwal N, et al. Dietary intake of antioxidant nutrients and the risk of incident Alzheimer disease in a biracial community study. *JAMA*. 2002;287(24):3230–7.
79. Grodstein F, Chen J, Willett WC. High-dose antioxidant supplements and cognitive function in community-dwelling elderly women. *Am J Clin Nutr*. 2003;77(4):975–84.
80. Zandi PP, Anthony JC, Khachaturian AS, Stone SV, Gustafson D, Tschanz JT, et al. Reduced risk of Alzheimer disease in users of antioxidant vitamin supplements: the Cache County Study. *Arch Neurol*. 2004;61(1):82–8.
81. Mendelsohn AB, Belle SH, Stoehr GP, Ganguli M. Use of antioxidant supplements and its association with cognitive function in a rural elderly cohort: the MoVIES Project. Monongahela Valley Independent Elders Survey. *Am J Epidemiol*. 1998;148(1):38–44.
82. Luchsinger JA, Tang MX, Shea S, Mayeux R. Antioxidant vitamin intake and risk of Alzheimer disease. *Arch Neurol*. 2003;60(2):203–8.
83. Fillenbaum GG, Kuchibhatla MN, Hanlon JT, Artz MB, Pieper CF, Schmadier KE, et al. Dementia and Alzheimer's disease in community-dwelling elders taking vitamin C and/or vitamin E. *Ann Pharmacother*. 2005;39(12):2009–14.
84. Gray SL, Anderson ML, Crane PK, Breitner JC, McCormick W, Bowen JD, et al. Antioxidant vitamin supplement use and risk of dementia or Alzheimer's disease in older adults. *J Am Geriatr Soc*. 2008;56(2):291–5.
85. Szeto HH. Development of mitochondria-targeted aromatic-cationic peptides for neurodegenerative diseases. *Ann N Y Acad Sci*. 2008;1147:112–21.
86. Jia YL, Wang W, Han N, Sun HL, Dong FM, Song YX, et al. The mitochondria-targeted small molecule SS31 delays progression of behavioral deficits by attenuating beta-amyloid plaque formation and mitochondrial/synaptic deterioration in APP/PS1 mice. *Biochem Biophys Res Commun*. 2023;658:36–43.
87. Manczak M, Mao P, Calkins MJ, Cornea A, Reddy AP, Murphy MP, et al. Mitochondria-targeted antioxidants protect against amyloid-beta toxicity in Alzheimer's disease neurons. *J Alzheimers Dis*. 2010;20(Suppl 2):S609–31.
88. Garcia-Alloza M, Borrelli LA, Hyman BT, Bacskai BJ. Antioxidants have a rapid and long-lasting effect on neuritic abnormalities in APP:PS1 mice. *Neurobiol Aging*. 2010;31(12):2058–68.
89. Perez-Gracia E, Torrejon-Escribano B, Ferrer I. Dystrophic neurites of senile plaques in Alzheimer's disease are deficient in cytochrome c oxidase. *Acta Neuropathol*. 2008;116(3):261–8.
90. Serrano-Pozo A, Betensky RA, Frosch MP, Hyman BT. Plaque-Associated Local Toxicity Increases over the Clinical Course of Alzheimer Disease. *Am J Pathol*. 2016;186(2):375–84.
91. Stern EA, Bacskai BJ, Hickey GA, Attenello FJ, Lombardo JA, Hyman BT. Cortical synaptic integration in vivo is disrupted by amyloid-beta plaques. *J Neurosci*. 2004;24(19):4535–40.
92. Yuan P, Zhang M, Tong L, Morse TM, McDougal RA, Ding H, et al. PLD3 affects axonal spheroids and network defects in Alzheimer's disease. *Nature*. 2022;612(7939):328–37.
93. Pratico D. Evidence of oxidative stress in Alzheimer's disease brain and antioxidant therapy: lights and shadows. *Ann N Y Acad Sci*. 2008;1147:70–8.
94. Mecocci P, Mariani E, Cornacchiola V, Polidori MC. Antioxidants for the treatment of mild cognitive impairment. *Neurol Res*. 2004;26(5):598–602.
95. Forman HJ, Zhang H. Targeting oxidative stress in disease: promise and limitations of antioxidant therapy. *Nat Rev Drug Discov*. 2021;20(9):689–709.
96. Galasko DR, Peskind E, Clark CM, Quinn JF, Ringman JM, Jicha GA, et al. Antioxidants for Alzheimer disease: a randomized clinical trial with cerebrospinal fluid biomarker measures. *Arch Neurol*. 2012;69(7):836–41.
97. Kryscio RJ, Abner EL, Caban-Holt A, Lovell M, Goodman P, Darke AK, et al. Association of Antioxidant Supplement Use and Dementia in the Prevention of Alzheimer's Disease by Vitamin E and Selenium Trial (PREADVISE). *JAMA Neurol*. 2017;74(5):567–73.
98. Mecocci P, Polidori MC. Antioxidant clinical trials in mild cognitive impairment and Alzheimer's disease. *Biochim Biophys Acta*. 2012;1822(5):631–8.

Publisher's Note

Springer Nature remains neutral with regard to jurisdictional claims in published maps and institutional affiliations.